Journal of Computational Physics **174,** 248–276 (2001)
doi:10.1006/jcph.2001.6904, available online at http://www.idealibrary.com on IDEAL®

Grid-Optimized Dispersion-Relation-Preserving Schemes on General Geometries for Computational Aeroacoustics

Cheolung Cheong* and Soogab Lee†

**Department of Aerospace Engineering, Seoul National University, BD 136-1318, Seoul 151-742, Korea; and*
†Center for Environmental Noise & Vibration Research, School of Mechanical and Aerospace Engineering, Seoul National University, BD 301-1303, Seoul 151-742, Korea
E-mail: accu99@snu.ac.kr, solee@plaza.snu.ac.kr

Received March 19, 2001; revised August 6, 2001

In this paper, we investigate the dispersion-relation-preserving property of a finite difference scheme on general geometries for computational aeroacoustics, where nondispersive and nondissipative properties are of critical importance. The analysis pertains to the application of the optimization algorithm of the dispersion-relation-preserving (DRP) scheme in wave number space to the general geometries—nonuniform Cartesian and curvilinear grids. In many computational aeroacoustics applications, the DRP schemes have often been favored for their accuracy and efficiency. DRP schemes, however, are implemented only on uniform Cartesian grids. Practical problems in aeroacoustics, however, are seldom confined to uniform Cartesian grids with the associated computing grids often being nonuniform Cartesian or curvilinear. Grid-optimized, dispersion-relation-preserving (GODRP) finite difference schemes are proposed, based on optimization that gives finite difference equations locally the same dispersion relation as the original partial differential equations on the grid points in the nonuniform Cartesian or curvilinear mesh. This local dispersion-relation-preserving property guarantees global accuracy of numerical schemes in the wave number space over the full domain. The basic idea behind mathematical formulations of GODRP schemes is that the optimization in the wave number space is carried out not on the computational domain but on the physical domain. Because the properties of Cartesian and curvilinear grids differ—whether the coupling of the coordinate variables between the physical and computational domains exists or not, different mathematical formulations are developed for each grid type. To investigate the effectiveness of GODRP schemes, a sequence of benchmark problems is executed. Through many numerical test problems, it is shown that the use of GODRP schemes can broaden the application area of conventional DRP schemes to aeroacoustic phenomena, enhancing both the speed and accuracy of the computation using nonuniform Cartesian or curvilinear grids.

0021-9991/01 $35.00

Key Words: high-order finite difference; dispersion-relation-preserving; computational aeroacoustics.

1. INTRODUCTION

In contrast with computational fluid dynamics (CFD), which has a history of fast development, computational aeroacoustics (CAA) has only recently emerged as a separate area of study. CAA focuses on the accurate prediction of aerodynamically generated sound as well as its propagation and far-field characteristics. Both aspects of the problem, sound generation and propagation, are enormously demanding in terms of time-domain computation due to the large number of grid points normally required. For aeroacoustic simulation to become more practical, CAA schemes must thus be higher order accurate and numerically optimized in order to reduce the required number of grid points per wavelength while still ensuring tolerable levels of numerically induced dissipation and dispersion.

Numerical dissipation and numerical dispersion are the two primary sources of error associated with computational schemes. Because of these errors, classical CFD schemes have been found to be unsatisfactory for the study of wave propagation over long distances and large time intervals. Many CFD schemes, such as the MacCormack scheme, upwind schemes, and essentially nonoscillatory (ENO) schemes have been extended to high order using more stencil points for application to acoustic problems [1–7]. Recent reviews of computational aeroacoustics by Tam [8] and Wells and Renaut [9] have discussed various numerical schemes currently popular in CAA. These include many compact and noncompact optimized schemes such as the family of high-order compact differencing schemes of Lele [10] and the DRP scheme of Tam and Webb [11]. They are all centered, nondissipative schemes, a property desirable for linear wave propagation. The DRP scheme is implemented by using a symmetric finite difference stencil on a uniform Cartesian grid. In this environment, the classic DRP schemes minimize numerical dispersion errors while producing essentially no dissipation errors. Unfortunately, there are two drawbacks to the classic DRP approach. First of all, practical problems in aeroacoustics are seldom confined to uniform Cartesian geometry, with the associated computational grids usually being nonuniform or curvilinear. Secondly, the inherent lack of numerical dissipation may result in spurious numerical oscillations and instability in practical applications. Recently, the low-dispersion finite volume scheme (LDFV) [12] and the optimized upwind DRP scheme (OUDRP) [13], which are a subset of the classical DRP scheme, have been presented in order to overcome the above-mentioned drawbacks. The former is constructed by applying an optimization algorithm, similar to the derivation process of the classic DRP scheme, to the interpolation formulae to compute the physical variables at the cell interface. The latter just utilizes the upwind-based finite difference for the optimization algorithm. The LDFV scheme is based on the finite volume method. The multidimensional finite volume algorithm is generally more expensive in terms of numerical cost than are finite difference algorithms [14]. Furthermore, numerical dispersion characteristics of the finite volume method are not as well developed mathematically as those of the finite difference method [12, 15]. This means that finite volume methods generally contain mathematical ambiguity in the optimization for low dispersion and dissipation schemes. The OUDRP is built based on general upwind finite difference methods. Being generally unsuitable for linear acoustic wave propagation due to their asymmetric stencil, upwind-based finite difference formulations have been favored less than central

difference ones [1, 16]. In addition, the OUDRP scheme is derived only on uniform Cartesian grids.

Some researchers [17, 18] have used the classical DRP scheme on curvilinear meshes for their numerical analysis. None of them, however, analyze the effect of curvilinear grids on the dispersion-relation-preserving property of the numerical scheme. Analysis of the effect is one of the motivations for this paper.

In this paper, grid-optimized dispersion-relation-preserving schemes (GODRP) are derived, which are designed to have locally the same dispersion relation as the partial differential equation and, at the same time, optimized dissipation characteristics at the given grids that are nonuniform Cartesian or curvilinear grids. To investigate the effectiveness of GODRP schemes, some benchmark problems are executed. Through the benchmark problems, the versatility of GODRP schemes will be proven which will widen the application area of the DRP scheme to various aeroacoustic problems, especially for nonuniform rectangular or curvilinear grids.

This paper is organized as follows. In Section 2, the derivation of the DRP scheme will be summarized. In Sections 3 and 4, mathematical formulation of GODRP schemes for nonuniform rectangular grids is described, followed by various benchmark problems used to evaluate the effectiveness of GODRP schemes for the rectangular grids. Because the coordinate variables in the physical domain of curvilinear grids are coupled with those of the computation domain, GODRP schemes for such grids call for different mathematical derivation than do those for the Cartesian grids. The derivation process of GODRP schemes for curvilinear grids is shown in Section 5. Two test simulations on curvilinear grids are then carried out to assess the accuracy of GODRP schemes for the curvilinear grids in Section 6. One is a simulation of acoustic wave propagation and the other of the scattering of acoustic pulses from a cylinder.

2. BRIEF REVIEW OF THE DRP SCHEME

Tam and Webb [11] have shown that if a given computational scheme and the governing equations have the same dispersion relations, then the numerical and exact solutions will have the same wave propagation characteristics and wave speeds. Accordingly, the classic DRP scheme, which essentially preserves the wave propagation characteristics of the governing equations, was developed. In this section, the mathematical derivation of the DRP scheme is reviewed briefly as follows.

Let the spatial derivative be approximated by a central difference scheme with a uniform mesh of spacing Δx as

$$\left(\frac{\partial u}{\partial x}\right)_j \approx \frac{1}{\Delta x}\sum_{l=-N}^{N} a_l u_{j+l}. \tag{1}$$

Now by applying a Fourier transform to the above equation and making use of the derivative and shifting theorems,

$$\begin{aligned} i\alpha\tilde{u} &\approx \frac{1}{\Delta x}\left[\sum_{l=-N}^{N} a_l e^{il\alpha\Delta x}\right]\tilde{u}, \\ &= i\bar{\alpha}\tilde{u} \end{aligned} \tag{2}$$

where $\tilde{u}$ is the spatial Fourier transform of u, and $\bar{\alpha}$ is an effective wave number of the finite difference scheme,

$$\bar{\alpha} = \frac{-i}{\Delta x} \sum_{l=-N}^{N} a_l e^{il\alpha\Delta x}, \tag{3}$$

where α is the actual wave number, and $i = \sqrt{-1}$.

Thus $\bar{\alpha}$ of Eq. (3) is seen as an approximation to the actual wave number α. Moreover, the nondimensional effective wave number $\bar{\alpha}\Delta x$ as a periodic function of $\alpha\Delta x$ with a period of 2π is a property of the finite difference scheme a_l. To assure that the Fourier transform of the finite difference scheme is a good approximation of the transform of the partial derivative over a certain wave number range, it is required that a_l be chosen to minimize the integrated error, E, over a certain wave number range, e, where

$$E = \int_0^e |\alpha\Delta x - \bar{\alpha}\Delta x|^2 \, d(\alpha\Delta x). \tag{4}$$

The conditions for E to be a minimum are

$$\frac{\partial E}{\partial a_l} = 0, \quad l = 1, 2, \ldots, N. \tag{5}$$

Equation (5) provides N equations for the N coefficients a_l, $l = 1, 2, \ldots, N$. It is possible to combine the truncated Taylor series method and the Fourier transform optimization method. It is well known that $\bar{\alpha}\Delta x$ approximates $\alpha\Delta x$ adequately for only a limited range of the long waves. The maximum resolvable wave number will be denoted by critical wave number $\bar{\alpha}_c$. In all the following numerical simulations for comparison, a seven-point stencil that can be obtained by minimizing Eq. (4) over the integral range $e = 1.1$ is used. The value is recommended by Tam and Webb [11].

3. MATHEMATICAL FORMULATION OF THE GODRP SCHEME FOR CARTESIAN GRIDS

For problems involving Cartesian grids, there is no coupling between the coordinate variables of the physical and computational domains, so this type of mesh can be approached with a one-dimensional formulation.

Consider the approximation of the first spatial derivative $\partial f/\partial x$ by the finite difference equation, which is given for a nonuniform grid of spacing Δx_i. Suppose n values of f both to the right and left of the point x are used in the finite difference equation where x is a continuous variable, i.e.,

$$\frac{\partial f}{\partial x} \approx \frac{1}{\overline{\Delta x}} \sum_{j=-n}^{n} a_j \, f(x + \Delta x_i \cdot \overline{\Delta x}). \tag{6}$$

Here, $\overline{\Delta x}$ is an averaged grid space and Δx_i is a normalized grid space. Each term is defined as follows (see Fig. 1):

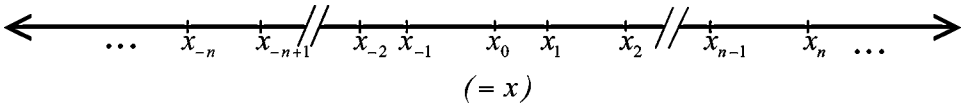

FIG. 1. Schematic diagram showing the $(2n+1)$-point stencil on a nonuniform grid.

$$\overline{\Delta x} = (x_n - x_{-n})/2n \tag{7}$$

$$\Delta x_i = (x_i - x_0)/\overline{\Delta x} (i = -n, -n+1, \ldots, n-1, n). \tag{8}$$

The Fourier transform and its inverse of a function are related by

$$\begin{aligned} \tilde{f}(\alpha) &= \frac{1}{2\pi} \int_{-\infty}^{\infty} f(x) e^{-i\alpha x}\, d\alpha \\ f(x) &= \int_{-\infty}^{\infty} \tilde{f}(\alpha) e^{i\alpha x}\, dx. \end{aligned} \tag{9}$$

Taking the Fourier transform of both sides of Eq. (6) yields

$$i\alpha \tilde{f} = \left(\frac{1}{\overline{\Delta x}} \sum_{j=-n}^{n} a_j e^{i\alpha \Delta x_i \cdot \overline{\Delta x}} \right) \tilde{f}. \tag{10}$$

Comparing the two sides of the above equation, it is clear that the quantity

$$\bar{\alpha} = \frac{-i}{\overline{\Delta x}} \sum_{j=-n}^{n} a_j e^{i\alpha \Delta x_i \cdot \overline{\Delta x}} \tag{11}$$

is the effective (or numerical) wave number of the Fourier transformation of the finite difference scheme over the nonuniform grids. It is evident that if the grid spaces are not symmetric, the effective wave number of Eq. (11), instead of being a real number as in the conventional DRP scheme, is a complex number. Thus, an optimization process must allow the values of $\bar{\alpha}_r \overline{\Delta x} - \alpha \overline{\Delta x}$ and $\bar{\alpha}_i \overline{\Delta x}$ to be as close to zero as possible for the designed range of wave numbers. Besides, the numerical stability of the scheme also has to be retained during the optimization process. Hence, such purpose can be achieved by minimizing the integrated error E, defined by the following:

$$\begin{aligned} E = &\int_0^{e_r} |\bar{\alpha}_r \overline{\Delta x} - \alpha \overline{\Delta x}|^2\, d(\alpha \overline{\Delta x}) \\ &+ \lambda \int_0^{e_i} \left| \bar{\alpha}_i \overline{\Delta x} + Sgn(c) \exp\left[-\ln 2 \cdot \left(\frac{\alpha \overline{\Delta x} - \pi}{\sigma} \right)^2 \right] \right|^2 d(\alpha \overline{\Delta x}). \end{aligned} \tag{12}$$

Here, the terms e_r, e_i denote the upper limits of the integration intervals of real and imaginary parts, respectively. The term λ is the weighting factor, σ is the half-width of a Gaussian function, and c is the speed of wave propagation in $u_t + cu_x = 0$.

It is possible to combine the traditional truncated Taylor series finite difference approximation and the wave number space approximation. To determine the coefficients of a

$2n+1$-point stencil GODRP spatial discretization, information about the computational grids must be given. By combining this information with the Taylor expansion, several constraint equations are obtained. If two coefficients to be used for the optimization are left, following $2n-1$ equations is an option.

$$\begin{bmatrix} 1 & 1 & 1 & 1 & 1 & 1 & 1 \\ \Delta_{n-2} & \Delta_{n-3} & \cdots & 0 & \Delta_{-1} & \cdots & \Delta_{-n} \\ \Delta_{n-2}^2 & \Delta_{n-3}^2 & \cdots & 0 & \Delta_{-1}^2 & \cdots & \Delta_{-n}^2 \\ \vdots & \vdots & \vdots & \vdots & \vdots & \vdots & \vdots \\ \Delta_{n-2}^{2n-2} & \Delta_{n-3}^{2n-2} & \cdots & 0 & \Delta_{-1}^{2n-2} & \cdots & \Delta_{-n}^{2n-2} \end{bmatrix} \begin{bmatrix} a_{n-2} \\ a_{n-3} \\ \vdots \\ a_0 \\ a_1 \\ \vdots \\ a_{-n} \end{bmatrix}$$

$$= \begin{bmatrix} -1 \\ -\Delta_n \\ -\Delta_n^2 \\ \vdots \\ -\Delta_n^{2n-2} \end{bmatrix} a_n + \begin{bmatrix} -1 \\ -\Delta_{n-1} \\ -\Delta_{n-1}^2 \\ \vdots \\ -\Delta_{n-1}^{2n-2} \end{bmatrix} a_{n-1} + \begin{bmatrix} 0 \\ 1 \\ 0 \\ \vdots \\ 0 \end{bmatrix}. \tag{13}$$

Here, Δ_i means Δx_i, which is defined in Eq. (8). The above equation can be recast into the following matrix form:

$$\boldsymbol{\Delta X} \cdot \boldsymbol{A} = \boldsymbol{C}_n a_n + \boldsymbol{C}_{n-1} a_{n-1} + \boldsymbol{C}_0. \tag{14}$$

By multiplying the inverse matrix of $\boldsymbol{\Delta X}$ by both the left- and right-hand sides of the equation, the following equation is obtained:

$$\boldsymbol{A} = \boldsymbol{\Delta X}^{-1} \boldsymbol{C}_n a_n + \boldsymbol{\Delta X}^{-1} \boldsymbol{C}_{n-1} a_{n-1} + \boldsymbol{\Delta X}^{-1} \boldsymbol{C}_0. \tag{15}$$

The above equation can be rewritten into the tensor form

$$a_j = \Delta C_{n,j} a_n + \Delta C_{n-1,j} a_{n-1} + \Delta C_{0,j}, \tag{16}$$

where $a_j = (\boldsymbol{A})_j$, $\Delta C_{n,j} = (\boldsymbol{\Delta X}^{-1} \boldsymbol{C}_n)_j$, $\Delta C_{n-1,j} = (\boldsymbol{\Delta X}^{-1} \boldsymbol{C}_{n-1})_j$, $\Delta C_{0,j} = (\boldsymbol{\Delta X}^{-1} \boldsymbol{C}_0)_j$, in which $(\boldsymbol{M})_j$ represents the *j-th* row element of the matrix $\boldsymbol{M}$.

By inserting Eq. (16) into Eq. (12) and minimizing Eq. (12), two linear algebraic equations, $\frac{\partial E}{\partial a_n} = 0$ and $\frac{\partial E}{\partial a_{n-1}}$ are obtained which determine the values of the coefficients a_n and a_{n-1}. Then the values of the other coefficients $a_j (j = -n, -n+1, \ldots, n-3, n-2)$ can be set by Eq. (16).

Figure 2 shows the real and imaginary parts of the effective wave number of the GODRP finite difference scheme for uniform grids using different optimization parameters, which are e_r, e_i, λ, and σ. Figure 2A depicts the real parts of the effective wave number, which approximates the wave number of the partial differential equation. As the values of e_r and e_i increase, the maximum values of the real parts of the effective wave numbers are also augmented. Figure 2B displays the imaginary parts of the effective wave number, which is the numerical damping affecting the numerical stability. The plots of the imaginary part conform to the designed shapes, which are Gaussian functions centered at $k\overline{\Delta x} = \pi$.

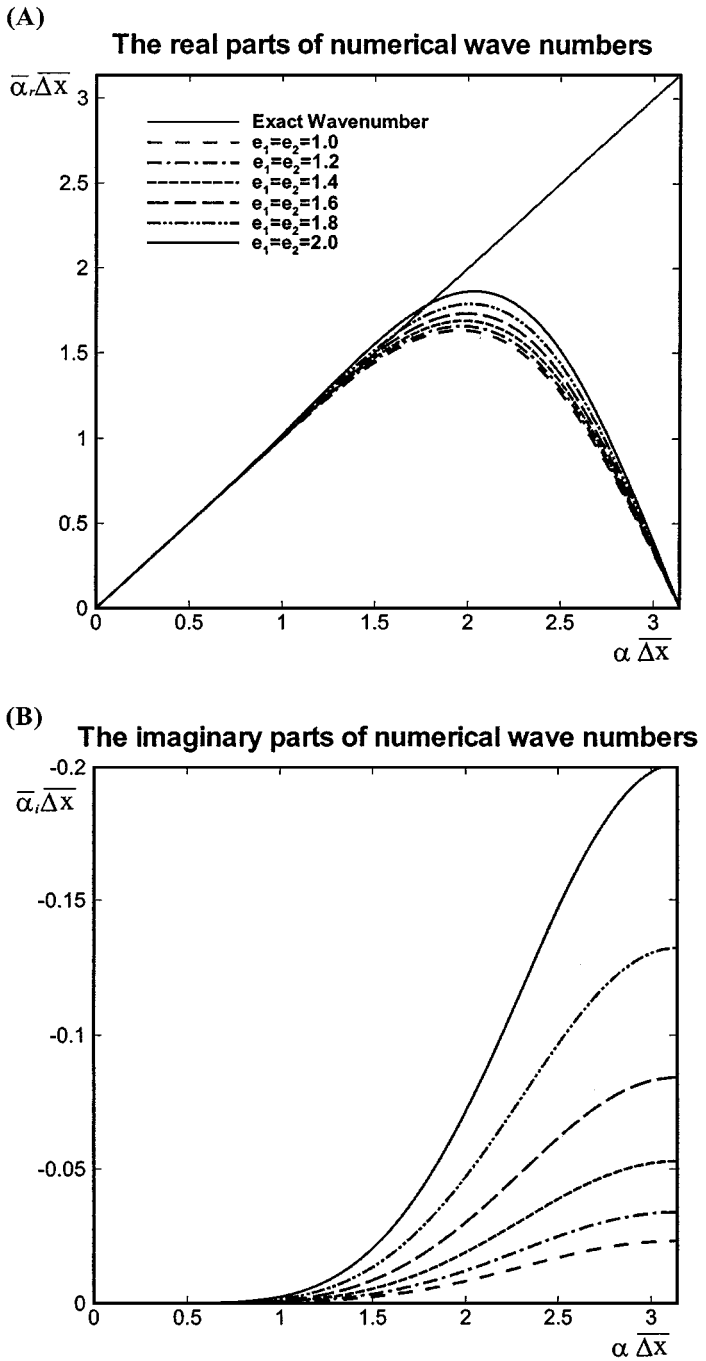

FIG. 2. Numerical wave number $\overline{\alpha}\overline{\Delta x}$ versus the exact wave number $\alpha\overline{\Delta x}$ for several values of e_r and e_i at $\lambda = 0.2$ and $\sigma = 0.2\pi$.

The Gaussian-shaped numerical damping terms are desirable in that they are small for long wave components, i.e., small $\alpha\overline{\Delta x}$, but large for short wave components, i.e., large $\alpha\overline{\Delta x}$. As the values of e_r and e_i increase, the maximum values for the imaginary parts at $\alpha\overline{\Delta x} = \pi$ are also increased.

TABLE I
Critical Wave Numbers at Various Values of e and σ with $\lambda = 0.2$

e	σ	$\overline{\alpha_c}\,\overline{\Delta x}$	Resolution (Points per wavelength)
1.0	0.15π	1.125	5.586
	0.20π	1.125	5.585
	0.25π	1.126	5.580
	0.30π	1.126	5.580
1.2	0.15π	1.219	5.154
	0.20π	1.217	5.162
	0.25π	1.220	5.150
	0.30π	1.220	5.150
1.4	0.15π	1.345	4.672
	0.20π	1.339	4.692
	0.25π	1.345	4.672
	0.30π	1.345	4.672
1.6	0.15π	0.853	7.366
	0.20π	0.846	7.425
	0.25π	0.853	7.366
	0.30π	0.853	7.366

Critical wave numbers that are the maximum resolvable wave numbers defined as $|\overline{\alpha_c \Delta x} - \alpha \overline{\Delta x}| < 0.005$ are listed in Table I for the various optimization parameters. As the values of e ($e_r = e_i$) increase up to 1.4, the critical wave number tends to increase. However, the critical wave number decreases over the range where the value of e exceeds 1.4. The values of the critical wave number are sensitive to the values of e but not to that of σ.

Based on this parameter study, it is recommended that the parameter e be assigned the value 1.4 for the maximum critical wave numbers when used in connection with the uniform grids. The other parameters are crucial to the imaginary parts of the numerical wave number. Thus, these values of the parameters are problem-dependent. Generally speaking, if a large damping is needed, the values of η and σ are increased to the values which do not generate the numerical instability. The opposite can be applied if a small damping is required. Similar analysis can be carried out for nonuniform grids. Through this analysis, optimization parameters can be determined.

4. NUMERICAL SIMULATIONS USING NONUNIFORM CARTESIAN GRIDS

Some CAA benchmark problems are solved with the GODRP scheme in order to estimate the effectiveness of the scheme. The governing equations are the linearized Euler equations. The radiation and outflow boundary conditions [19] are applied at the far-field boundary of the computational domain. Wall boundary conditions are applied with ghost values of pressure at the ghost points [20]. Numerical results are compared with analytic solutions and (or) those from the classical DRP scheme on uniform Cartesian grids. The standard four-step Runge–Kutta method or an optimized Adams–Bashford method [11] is used as the numerical time-integration scheme. Unless otherwise noted, a seven-point stencil of the GODRP and DRP schemes is used in all the following numerical computations.

4.1. First Order Linear Wave Propagation

The GODRP scheme is applied to solve first order linear wave propagation through several types of grids defined as follows:

(A) regular spacing: $\Delta x = 1.0\ (-50 \le x \le 50)$;
(B) regularly perturbed spacing: $x(I) = (I - 51) + (-1)^I \times (0.1)(-50 \le I \le 50)$;
(C) smoothly stretching: $\Delta x_1 = 0.5\ (x \le 0)$, $\Delta x_I = 0.1 \times I + 0.5(I = 2, \ldots, 5)$, $\Delta x_6 = 1.0\ (x \ge 3)$;
(D) suddenly coarsened mesh: $\Delta x = 0.5\ (x \le 0\ )$, $\Delta x = 1.0\ (x \ge 0)$.

Figure 3 gives a comparison between the exact solutions and the numerical solutions for the GODRP scheme on each grid at a given time instant. In all cases, the time step Δt is 0.1, initial wave distributions are given by the Gaussian function $\exp(-\ln 2 \cdot (x - x_0)^2/4^2)$, and periodic boundary conditions are applied to both ends of the computational domain. Excellent agreement between the computed results of the GODRP scheme and the exact solution is shown for each grid type. To highlight the effectiveness of the GODRP scheme for the suddenly coarsened mesh, which is a main concern from a practical point of view, the propagation of a disturbance on this type of mesh is shown in Fig. 3D. An analysis of the behavior of a smooth solution as it passes through a sudden mesh coarsening has been presented by Vichnevetsky [21] for a 1-D advection equation, semidiscretized with the standard second-order centered scheme. This analysis indicates that although the total energy is preserved, a significant portion of the energy is deposited at the grid-coarsened interface on a reflected solution composed primarily of odd–even modes and modulated by a smooth envelope. This reflected energy propagates upstream (i.e., with negative group velocity) and in most circumstances, if left unchecked, has the potential to ultimately contaminate the genuine solution. Such phenomena, however, cannot be found for the solution of the GODRP scheme if the coarsened grid sufficiently resolves the smooth solution.

4.2. Two-Dimensional Pulse

The problems of propagation and reflection off a solid wall of a 2-D pulse in the presence of irregular grid spaces are considered next. These problems were the first CAA benchmark problems to be provided in [1]. First, 2-D wave propagation problems are investigated. The solutions were initialized at $t = 0$ by prescribing acoustic, vorticity, and entropy disturbances of the form

$$
\begin{aligned}
p &= \exp\left[-\ln 2 \cdot \left(\frac{x^2 + y^2}{r_1^2}\right)\right] \\
\rho &= \exp\left[-\ln 2 \cdot \left(\frac{x^2 + y^2}{r_1^2}\right)\right] + 0.1 \exp\left[-\ln 2 \cdot \left(\frac{(x - x_0)^2 + y^2}{r_2^2}\right)\right] \\
u &= 0.04y \exp\left[-\ln 2 \cdot \left(\frac{(x - x_0)^2 + y^2}{r_2^2}\right)\right] \\
v &= 0.04(x - x_0) \exp\left[-\ln 2 \cdot \left(\frac{(x - x_0)^2 + y^2}{r_2^2}\right)\right].
\end{aligned}
\tag{17}
$$

Here, $r_1 = 3$, $r_2 = 5$, and $x_0 = 67$.

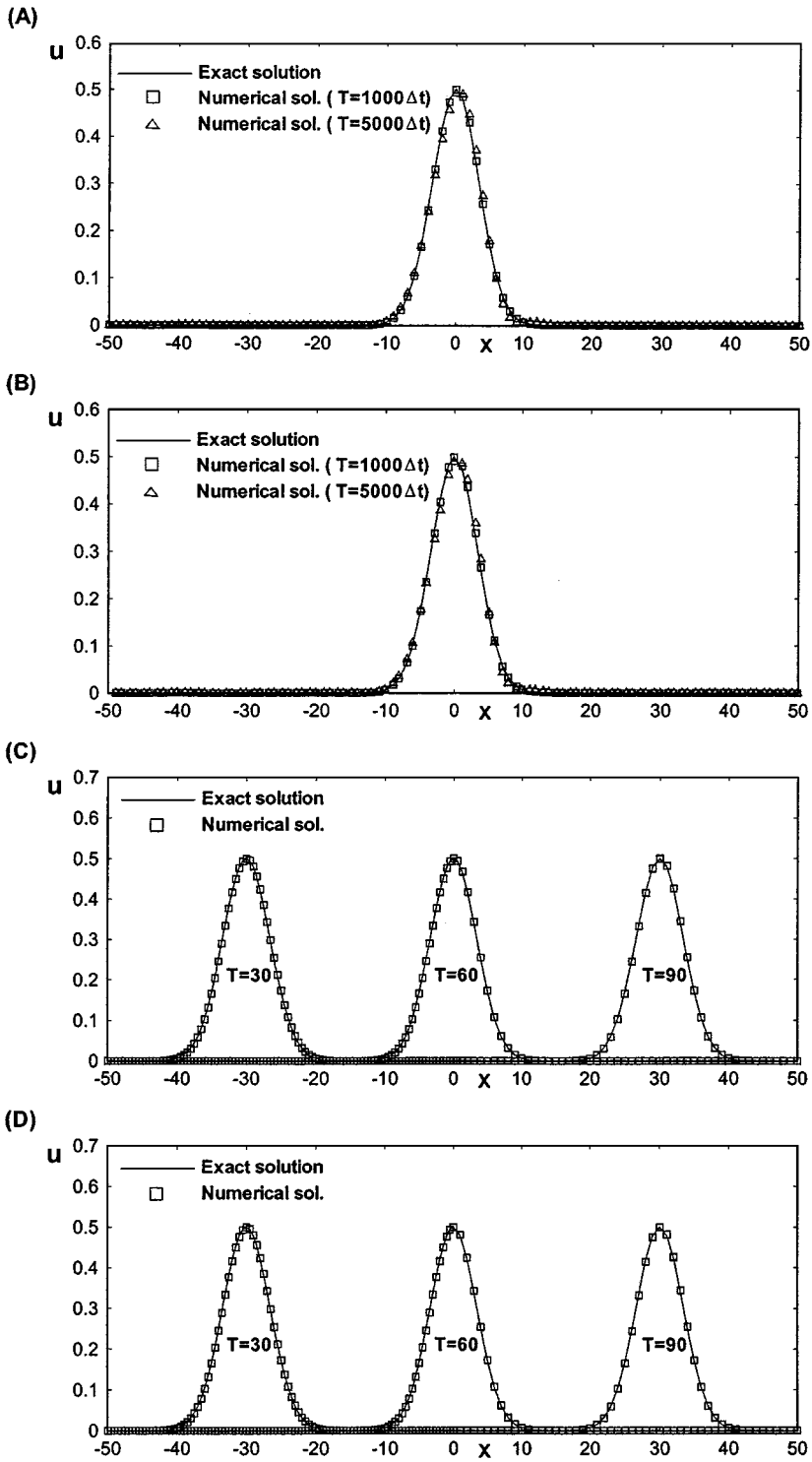

FIG. 3. Solutions of the first-order wave equation for several grids: (A) uniform grids; (B) regularly perturbed grids; (C) smoothly stretching grids; (D) sudden coarsened grids.

One of the two meshes shown in Fig. 4A is a uniform one used for the classical DRP scheme and the other is the nonuniform one for the GODRP scheme. The nonuniform grids are generated by $x(i) = i - 101 + (-1)^i \cdot (-0.1)(i = 1, \ldots, 201)$, and $y(j) = j - 101 + (-1)^j \cdot (-0.1)(j = 1, \ldots, 201)$. Figure 4B shows the computed density contours at $t = 30$ and $t = 60$. The exact solution is shown in dotted lines. Figure 4C gives the computed density waveforms and the exact solution at $t = 30$ and $t = 60$ along the line $y = 0$. At $t = 30$, the acoustic pulse and the entropy pulse are separated from each other. At $t = 60$, the acoustic pulse catches up and merges with the entropy pulse. An examination of Figs. 4B and C reveals that the numerical results from using both GODRP and classical DRP show good agreement with the exact solutions.

A second problem is the reflection of an acoustic pulse off a wall in the presence of a uniform flow in semiinfinite space. The wall is at $y = 0$. The initial condition is as follows:

$$u = v = 0$$
$$p = \rho = \exp\left[-\ln 2 \cdot \left(\frac{x^2 + (y - y_0)^2}{r^2}\right)\right]. \tag{18}$$

Here, $y_0 = 25$ and $r = 3$.

Figure 5A shows the uniform mesh used for the classic DRP scheme and the nonuniform one used for the GODRP scheme, which is clustered near the wall with an abruptly grid-coarsened interface ($\Delta y_2 = 2\Delta y_1$) at $y = 4$. The density distributions in Fig. 5B show good agreement with each other. A detailed analysis of the reflection of an acoustic wave from a wall using a solid wall boundary condition by means of ghost values has been carried out by Tam and Dong [20]. They show that in addition to the reflected acoustic wave, spurious waves are reflected. Furthermore, the spatially damped numerical waves of the computation scheme are also excited at the wall boundary. These waves form a numerical boundary layer. Figure 6 shows their numerical analysis on the numerical boundary layers. Figure 6A shows the calculated numerical boundary layer thickness as a function of the angle of incidence with a spatial resolution of $\lambda/\Delta x = 6$. It is found that the numerical boundary layer is the thickest for normal incidence. Figure 6B shows the corresponding numerical boundary layer thickness in the case of a spatial resolution of $\lambda/\Delta x = 6$. It is clear that with finer spatial resolution the numerical boundary layer thickness decreases. Figure 6C shows the dependence of the magnitude of the reflected parasite wave on the angle of incidence for various spatial resolutions. The magnitude of the reflected parasite wave would greatly be reduced if the spatial resolution in the computation were increased. From their conclusion, it is evident that the ability of the GODRP scheme to facilitate nonuniform grids, such as that in Fig. 5, enables one to avoid the inefficiency of using a much greater number of grids in the whole computational domain, as does the conventional DRP scheme, to reduce the numerical boundary layer thickness and the magnitude of the reflected parasite wave.

4.3. Acoustic Radiation from an Oscillating Circular Cylinder in a Wall

This problem is also provided as one of the first CAA benchmark problems. The governing equations for the r–x plane where (r, x, θ) are the cylindrical coordinates with the origin at the center of the piston are as follows:

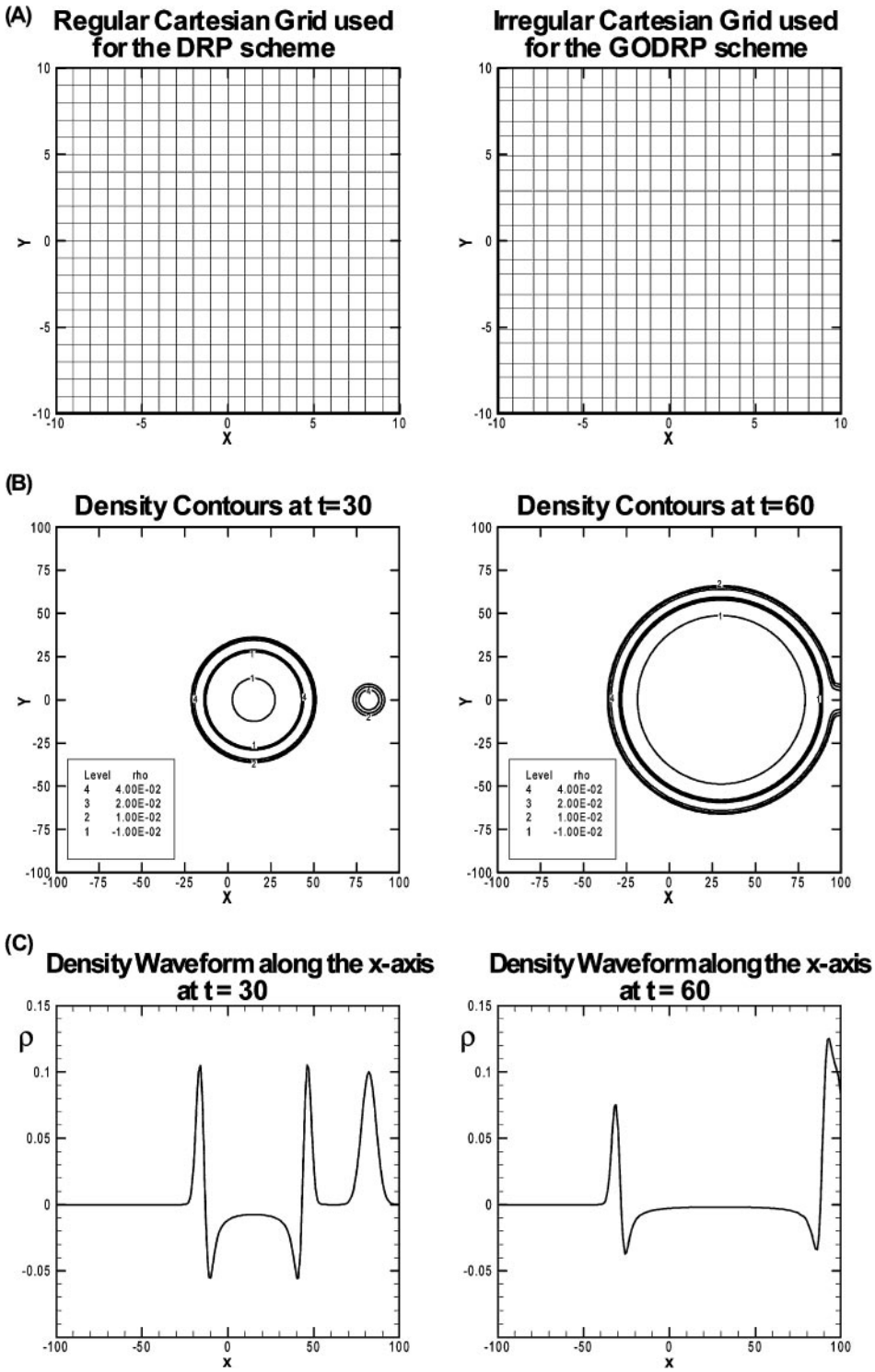

FIG. 4. Comparison of the numerical results by using GODRP and DRP schemes for a wave propagation problem (GODRP, —; DRP, –·–; exact, ----).

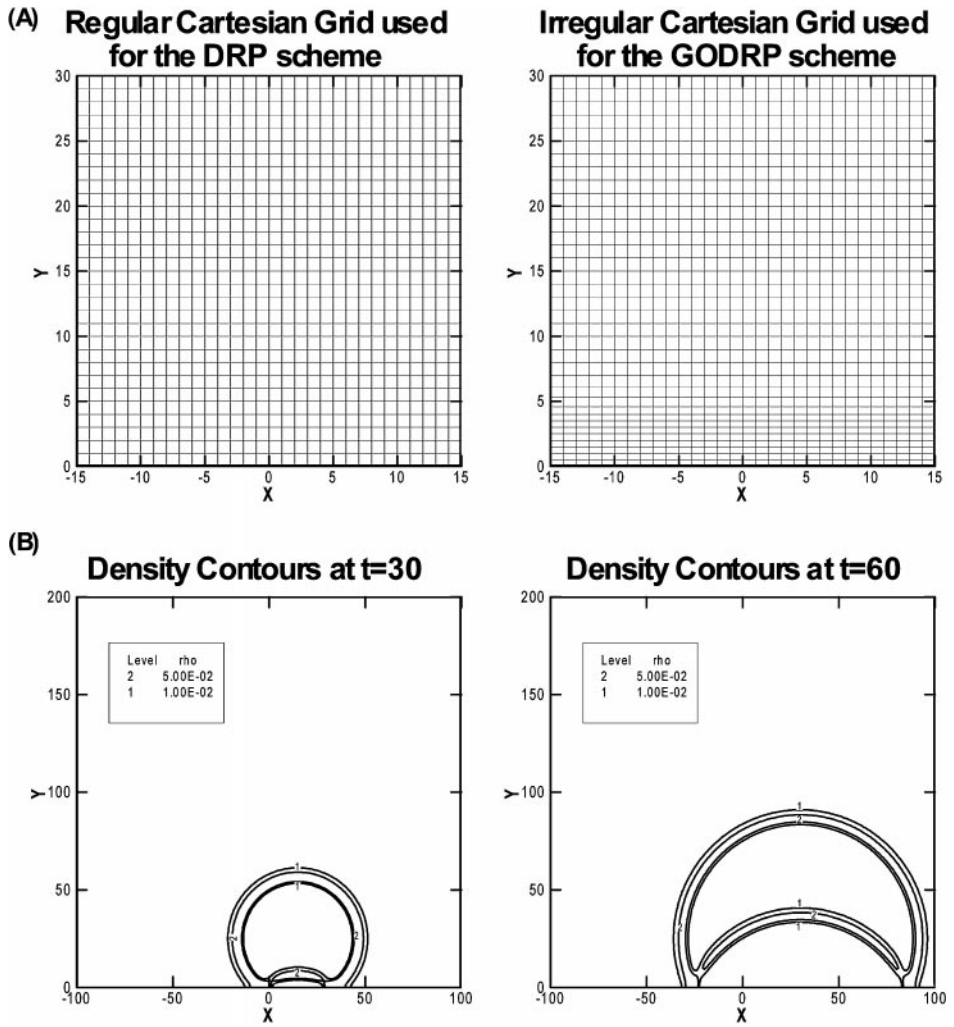

FIG. 5. Comparison of the numerical results from a GODRP and a DRP scheme for reflection of an acoustic wave from a wall (GODRP, —; DRP, –·–; exact, ----).

$$\begin{aligned}
\frac{\partial u}{\partial t} + \frac{\partial p}{\partial x} &= 0, \\
\frac{\partial v}{\partial t} + \frac{\partial p}{\partial y} &= 0, \\
\frac{\partial p}{\partial t} + \frac{\partial v}{\partial r} + \frac{v}{r} + \frac{\partial u}{\partial x} &= 0.
\end{aligned} \tag{19}$$

The computational domain and boundary conditions are shown in Fig. 7. The normal velocity of the piston is set to be $u = \varepsilon_0 \sin \omega t$. The amplitude and angular frequency are set to be 10^{-4} and 0.2π, respectively. The radius of the piston equals 10. The computation domain is $0 \le x \le 100$, $0 \le r \le 100$.

At the axis of symmetry, $r = 0$, the above equation is singular. In order to eliminate this singularity, the term v/r of Eq. (19) is replaced with $\partial v/\partial r$ since as $r \to 0$, $v \to 0$.

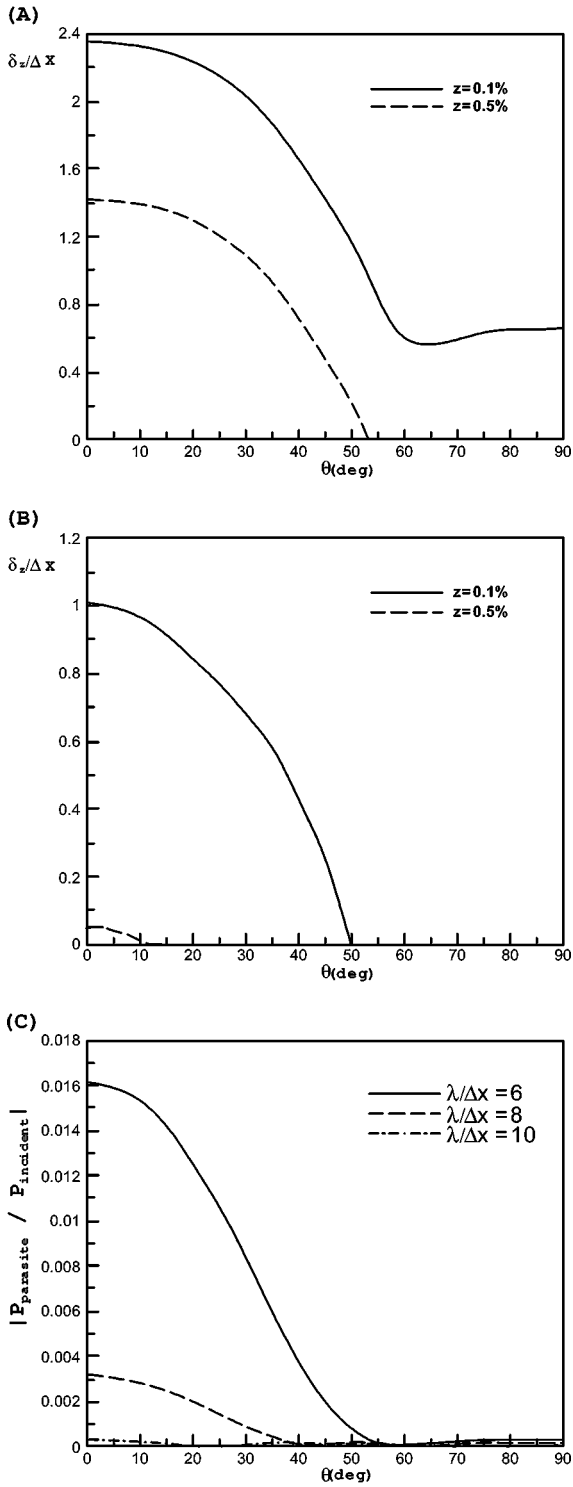

FIG. 6. Thickness of numerical boundary layer; (A) $\lambda/\Delta x = 6$; (B) $\lambda/\Delta x = 10$; and magnitude of the reflected parasite wave, (C), as a function of the angle of incidence. (δ_z = distance between the wall and the point where the spurious numerical solution drops to z times the magnitude of the reflected acoustic wave amplitude.)

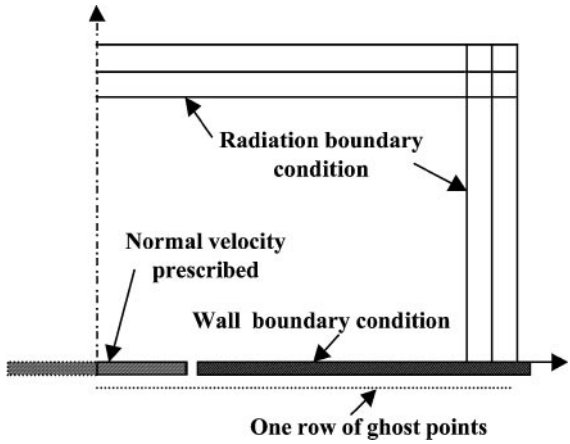

FIG. 7. The computational domain and boundary conditions for numerical simulations.

However, there is a sudden change in the governing finite difference equations between the first two columns of mesh points on the left side of the computational domain. In addition, a discontinuity in the boundary condition at the edge of the piston is present. These two discontinuities generate short-wavelength spurious numerical waves. This is thus a good benchmark problem, where the numerical scheme's ability to suppress such spurious waves can be tested. Figures 8A and B show pressure contours of $p = 0$ from classic DRP and GODRP schemes for the beginning of a cycle. For an unbiased comparison, the same regular mesh ($\Delta r = \Delta x = 1$) is used for both schemes. The quality of the solution of the classical DRP scheme is degraded by oscillation produced by spurious waves. The spurious waves are mainly due to above-mentioned discontinuities (see [22] for a more detailed

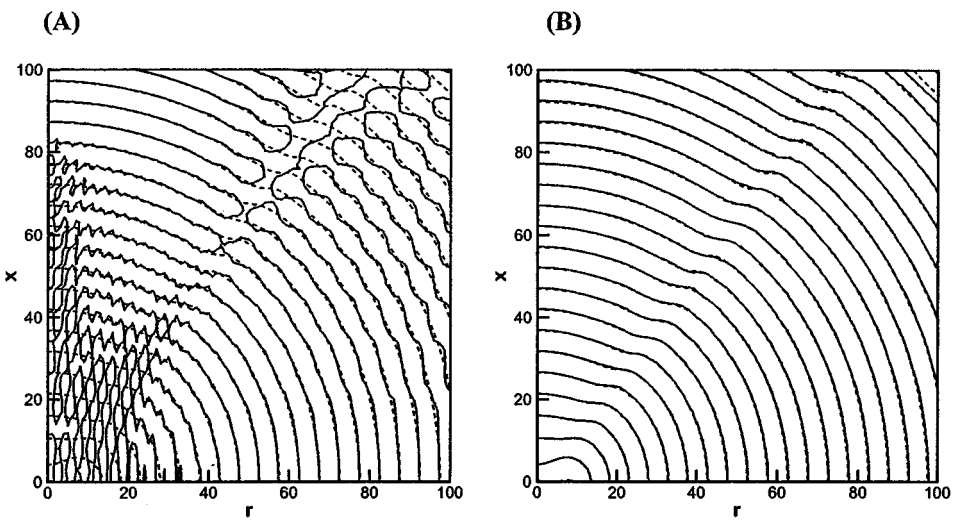

FIG. 8. Pressure contour ($p = 0$) at $t = 140$ within full computational domain. (a) DRP scheme without damping terms; (b) GODRP scheme (exact soluton, ----; numerical solution, —).

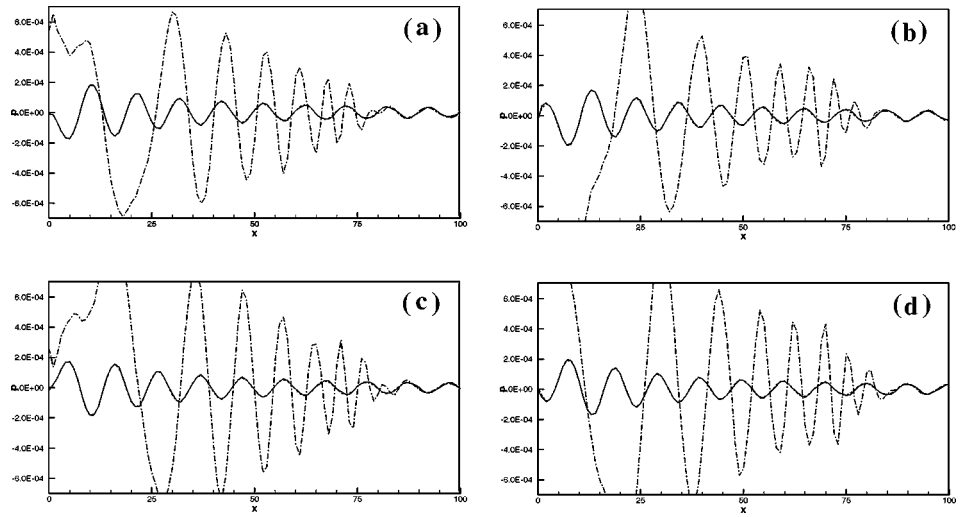

FIG. 9. Pressure distribution along the axis of the piston at (a) one quarter of a cycle, (b) a half cycle, (c) three quarters of a cycle, (d) the beginning of a cycle (exact, ----; DRP, –·–; GODRP, —).

description). The conventional DRP scheme does not have an intrinsic damping to suppress such spurious waves. In contrast with the result from the DRP scheme, the solution from the GODRP scheme shows good agreement with the exact solution. The pressure distributions along the axis of symmetry ($r = 0$) at the beginning of a cycle, at one quarter of a cycle, at a half cycle, and at three quarters of a cycle are shown in Fig. 9. As can be seen from the figure, the agreement of the results from the GODRP scheme with the exact solution is very good. The results from the DRP scheme without damping terms show poor agreement with those of the exact solution.

5. MATHEMATICAL FORMULATION OF GODRP SCHEMES FOR CURVILINEAR GRIDS

Different mathematical derivations of GODRP schemes are needed for curvilinear grids than for Cartesian grids because the coordinate variables ξ and η in the computation domain are coupled with x and y in the physical domain. In order to develop the mathematical formulation of GODRP schemes for curvilinear grids, the derivatives $\partial f/\partial x$ and $\partial f/\partial y$ in the physical domain are considered and cast in a strong conservative form by introducing a general curvilinear coordinate transformation $(x, y) \to (\xi, \eta)$ as follows (see Fig. 10):

$$\begin{aligned} \frac{1}{J}\frac{\partial f}{\partial x} &= \frac{\partial}{\partial \xi}(y_\eta f) - \frac{\partial}{\partial \eta}(y_\xi f) \\ \frac{1}{J}\frac{\partial f}{\partial y} &= -\frac{\partial}{\partial \xi}(x_\eta f) + \frac{\partial}{\partial \eta}(x_\xi f). \end{aligned} \tag{20}$$

Suppose $(2n + 1)$-point central stencils are used to approximate the derivatives of ξ and η

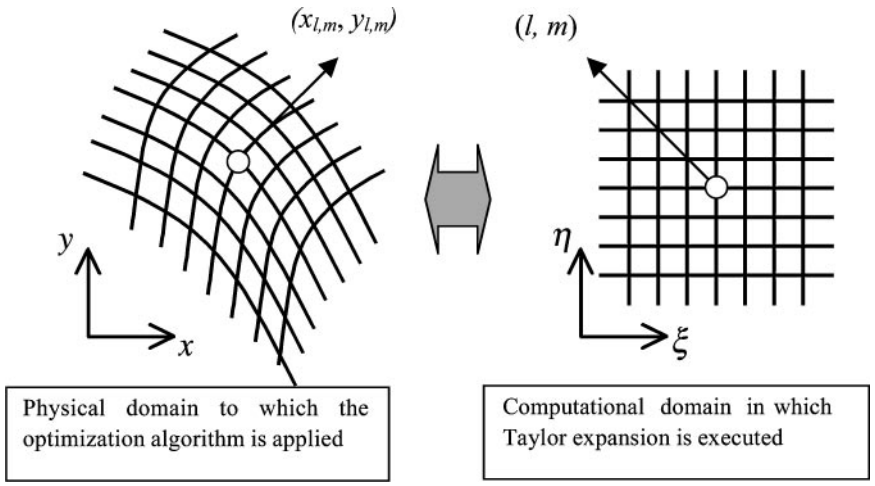

FIG. 10. Schematic diagram showing a general curvilinear coordinate transformation between the physical and computational domains in which the optimization and Taylor expansion are carried out, respectively.

in the (l, m) points of the right-hand side of Eq. (20):

$$\begin{aligned}\frac{1}{J}\frac{\partial f}{\partial x} &\approx \sum_{j=-n}^{n} a_j (y_\eta)_{l+j,m}\, f_{l+j,m} - \sum_{j=-n}^{n} a_j (y_\xi)_{l,m+j}\, f_{l,m+j} \\ \frac{1}{J}\frac{\partial f}{\partial y} &\approx -\sum_{j=-n}^{n} a_j (x_\eta)_{l+j,m}\, f_{l+j,m} + \sum_{j=-n}^{n} a_j (x_\xi)_{l,m+j}\, f_{l,m+j}.\end{aligned} \tag{21}$$

Assume that $f(x, y) = \bar{f} e^{i(\alpha x+\beta y)}$ and insert this form into Eq. (21):

$$\begin{aligned}\frac{i\alpha}{J}\bar{f} e^{i(\alpha x+\beta y)} &\approx \sum_{j=-n}^{n} a_j (y_\eta)_{l+j,m}\, \bar{f} e^{i(\alpha x_{l+j,m}+\beta y_{l+j,m})} - \sum_{j=-n}^{n} a_j (y_\xi)_{l,m+j}\, \bar{f} e^{i(\alpha x_{l,m+j}+\beta y_{l,m+j})} \\ \frac{i\beta}{J}\bar{f} e^{i(\alpha x+\beta y)} &\approx -\sum_{j=-n}^{n} a_j (x_\eta)_{l+j,m}\, \bar{f} e^{i(\alpha x_{l+j,m}+\beta y_{l+j,m})} + \sum_{j=-n}^{n} a_j (x_\xi)_{l,m+j}\, \bar{f} e^{i(\alpha x_{l,m+j}+\beta y_{l,m+j})}.\end{aligned} \tag{22}$$

Comparing the two sides of Eq. (22), it is evident that the quantities

$$\begin{aligned}\bar{\alpha} &= J \cdot \left[\sum_{j=-n}^{n} a_j (y_\eta)_{l+j,m} e^{i(\alpha \Delta x_{l+j,m}\overline{\Delta x}+\beta \Delta y_{l+j,m}\overline{\Delta y})} \right. \\ &\qquad \left. - \sum_{j=-n}^{n} a_j (y_\xi)_{l,m+j} e^{i(\alpha \Delta x_{l,m+j}\overline{\Delta x}+\beta \Delta y_{l,m+j}\overline{\Delta y})} \right], \\ \bar{\beta} &= J \cdot \left[-\sum_{j=-n}^{n} a_j (x_\eta)_{l+j,m}\, \bar{f} e^{i(\alpha \Delta x_{l+j,m}\overline{\Delta x}+\beta \Delta y_{l+j,m}\overline{\Delta y})} \right. \\ &\qquad \left. + \sum_{j=-n}^{n} a_j (x_\xi)_{l,m+j}\, \bar{f} e^{i(\alpha \Delta x_{l,m+j}\overline{\Delta x}+\beta \Delta y_{l,m+j}\overline{\Delta y})} \right]\end{aligned} \tag{23}$$

are the effective wave numbers of the finite difference scheme in the x and y directions, respectively. The Δx and Δy are normalized grid spaces identical to those in Eq. (8). $\overline{\Delta x}$ and $\overline{\Delta y}$ are averaged grid spaces, defined as follows:

$$\overline{\Delta x} = (\Delta x_{\max} - \Delta x_{\min})/2n,\ \overline{\Delta y} = (\Delta y_{\max} - \Delta y_{\min})/2n. \tag{24}$$

Here, $\Delta x_{\max} = MAX(\Delta x_{\max,\xi}, \Delta x_{\max,\eta})$, $\Delta y_{\max} = MAX(\Delta y_{\max,\xi}, \Delta y_{\max,\eta})$

$$\begin{aligned}
\Delta x_{\min} &= MAX(\Delta x_{\min,\xi}, \Delta x_{\min,\eta}), \quad \Delta y_{\min} = MAX(\Delta y_{\min,\xi}, \Delta y_{\min,\eta}) \\
\Delta x_{\max,\xi} &= MAX(x_{l-n,m} - x_{l,m}, x_{l-n+1,m} - x_{l,m}, \ldots, x_{l+n-1,m} - x_{l,m}, x_{l+n,m} - x_{l,m}) \\
\Delta x_{\max,\eta} &= MAX(x_{l,m-n} - x_{l,m}, x_{l,m-n+1} - x_{l,m}, \ldots, x_{l,m+n-1} - x_{l,m}, x_{l,m+n} - x_{l,m}) \\
\Delta y_{\max,\xi} &= MAX(y_{l-n,m} - y_{l,m}, y_{l-n+1,m} - y_{l,m}, \ldots, y_{l+n-1,m} - y_{l,m}, y_{l+n,m} - y_{l,m}) \\
\Delta y_{\max,\eta} &= MAX(y_{l,m-n} - y_{l,m}, y_{l,m-n+1} - y_{l,m}, \ldots, y_{l,m+n-1} - y_{l,m}, y_{l,m+n} - y_{l,m}) \\
\Delta x_{\min,\xi} &= MIN(x_{l-n,m} - x_{l,m}, x_{l-n+1,m} - x_{l,m}, \ldots, x_{l+n-1,m} - x_{l,m}, x_{l+n,m} - x_{l,m}) \\
\Delta x_{\min,\eta} &= MIN(x_{l,m-n} - x_{l,m}, x_{l,m-n+1} - x_{l,m}, \ldots, x_{l,m+n-1} - x_{l,m}, x_{l,m+n} - x_{l,m}) \\
\Delta y_{\min,\xi} &= MIN(y_{l-n,m} - y_{l,m}, y_{l-n+1,m} - y_{l,m}, \ldots, y_{l+n-1,m} - y_{l,m}, y_{l+n,m} - y_{l,m}) \\
\Delta y_{\min,\eta} &= MIN(y_{l,m-n} - y_{l,m}, y_{l,m-n+1} - y_{l,m}, \ldots, y_{l,m+n-1} - y_{l,m}, y_{l,m+n} - y_{l,m}).
\end{aligned}$$

It is clear that if the values of y_η, y_ξ, x_η, and x_ξ are not symmetric, the effective wave numbers of Eq. (23) are not real numbers but complex numbers. Thus, an optimization process must allow the values of $\bar{\alpha}_r\overline{\Delta x} - \alpha\overline{\Delta x}$, $\bar{\beta}_r\overline{\Delta y} - \beta\overline{\Delta y}$, $\bar{\alpha}_i\overline{\Delta x}$, and $\bar{\beta}_i\overline{\Delta y}$ to be as close to zero as possible for a designated range of wave numbers. For the optimization of the numerical wave numbers, the integrated error E is defined as follows:

$$\begin{aligned}
E = &\int_0^R \int_0^\pi \lfloor(\bar{\alpha}_r\overline{\Delta x} - \alpha\overline{\Delta x})^2 + (\bar{\beta}_r\overline{\Delta y} - \beta\overline{\Delta y})^2\rfloor\, r\, d(\theta)\, d(r) \\
&+ \lambda \int_0^R \int_0^\pi [\bar{\alpha}_i\overline{\Delta x} + \bar{\beta}_i\overline{\Delta y} + A \cdot \exp(-\ln 2 \cdot (r-\pi)^2/\sigma^2)]^2 r\, d(\theta)\, d(r).
\end{aligned} \tag{25}$$

Here, $r = \sqrt{(\alpha\overline{\Delta x})^2 + (\beta\overline{\Delta y})^2}$, $\theta = \tan^{-1}(\beta\overline{\Delta y}/\alpha\overline{\Delta x})$. The terms R denote the upper limits of the integration variable r; λ is the weighting factor; A is the amplitude of the Gaussian function; and σ is the half-width of the Gaussian function. By minimizing the integrated error E, the values of the coefficients a_j can be determined. GODRP schemes on the curvilinear grids can be constructed by combining the above optimization in the physical domain and the traditional truncated Taylor series finite difference approximation in the computational domain (see Fig. 10). The detailed mathematical algorithm for the determination of the coefficients of the GODRP scheme on curvilinear grids is given in the Appendix.

Figure 11 presents the sample grids to which the grid-optimization algorithm is applied and the comparisons of the numerical wave numbers of the GODRP and DRP schemes. The mesh shown in Fig. 11A is generated analytically according to the expression

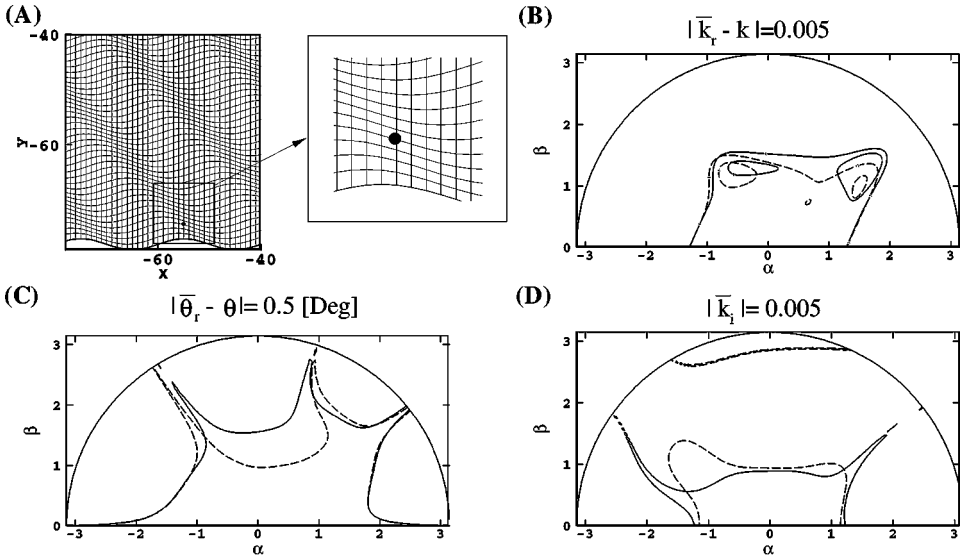

FIG. 11. Curvilinear grid and the comparison of numerical wave numbers between the GODRP scheme and the DRP scheme. (Optimization parameters: $R = 0.4\pi$, $\lambda = 0.07$. GODRP, —; DRP, ----). (A) Grid points for which grid optimization algorithm is applied. (B) The magnitude errors of the real parts of the numerical wave numbers; ($\bar{k}_r = \sqrt{\mathrm{Re}(\bar{\alpha})^2 + \mathrm{Re}(\bar{\beta})^2}$, $k = \sqrt{\alpha^2 + \beta^2}$). (C) The propagation direction errors of the real parts of the numerical wave numbers; ($\bar{\theta}_r = \tan^{-1}(\mathrm{Re}(\bar{\beta}_r)/\mathrm{Re}(\bar{\alpha}_r))$, $\theta = \tan^{-1}(\beta/\alpha)$). (D) The absolute values of the imaginary parts of the numerical wave numbers defined as $|\bar{k}_i| = |\mathrm{Im}(\bar{\alpha}_i + \bar{\beta}_i)|$.

$$
\begin{aligned}
x_{l,m} &= x_{\min} + \Delta x(l-1) \\
y_{l,m} &= y_{\min} + \Delta y\,[(m-1) + A\sin(2\pi/\lambda \cdot (x + Pj))]\,,
\end{aligned}
\tag{26}
$$

where the amplitude, wavelength, and phase shift parameters are specified as $A = 1, \lambda = 20$, and $P = 1$. Grid lengths, Δx, and Δy are set to be unity. Figures 11B, C, and D show the differences of the absolute values of the real parts, the propagating angle of the real parts, and the absolute values of the imaginary parts between the numerical and exact wave numbers, respectively. It can be observed that the numerical wave numbers of GODRP schemes reveal smaller errors with the exact wave number than those of the DRP schemes. To make this figure easier to understand, comparisons of the numerical wave numbers and exact wave numbers are shown at the line $\theta = 45^\circ$ of Fig. 11 in Fig. 12. One can more easily understand the results of the grid-optimized algorithm with the aid of this figure. For a more quantitative comparison between the numerical wave numbers from the GODRP and the DRP schemes, Table II shows the averaged errors of the numerical wave numbers with the exact wave number. It is found that the averaged errors of the GODRP scheme are of lower magnitude than those of the DRP schemes.

6. NUMERICAL SIMULATIONS USING CURVILINEAR GRIDS

Two test problems are executed to assess the effectiveness of GODRP schemes for curvilinear grids. One is on acoustic wave propagation and the other is on the scattering of acoustic pulses from a cylinder. The linearized, two-dimensional, compressible Euler equations are

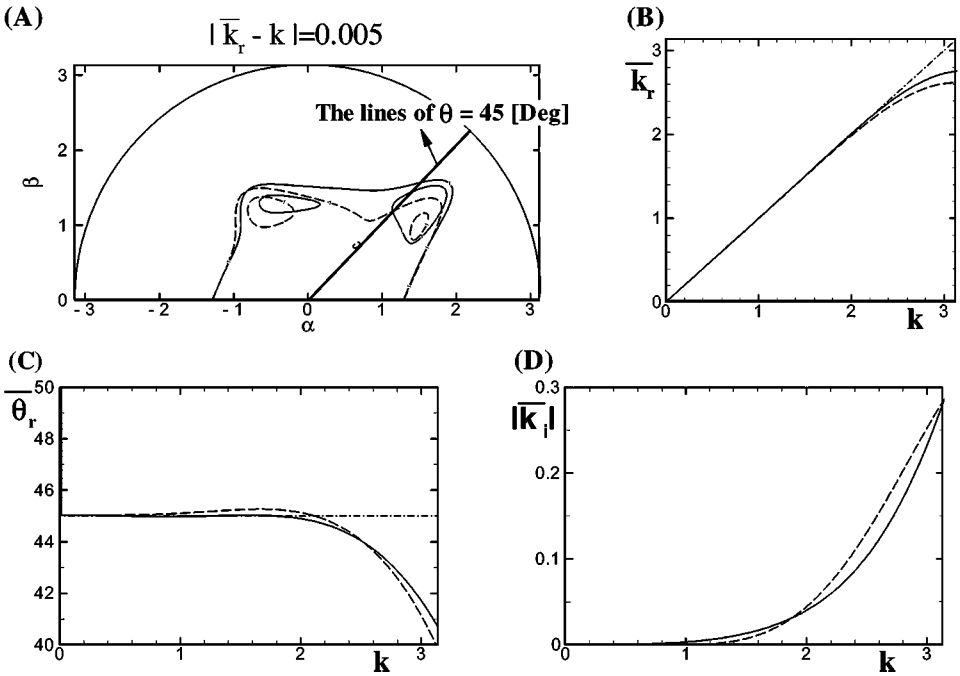

FIG. 12. Comparison of the numerical wave numbers at the lines $\theta = 45^\circ$. (Exact wave number, –·–·–; GODRP, —; DRP, ----).

considered in generalized curvilinear coordinates

$$\frac{\partial \hat{U}}{\partial t} = -R(\hat{U}), \quad \text{where } R(\hat{U}) = \frac{\partial \hat{E}}{\partial \xi} + \frac{\partial \hat{F}}{\partial \eta}. \tag{27}$$

The primitive variables, $\hat{U}$, and the transformed fluxes, $\hat{E}$ and $\hat{F}$, are as follows:

$$\hat{U} = \frac{1}{J}[\rho \;\; u \;\; v \;\; p]^t, \quad \hat{E} = \frac{1}{J}[\xi_x E + \xi_y F], \quad \hat{F} = \frac{1}{J}[\eta_x E + \eta_y F]. \tag{28}$$

TABLE II
Quantitative Comparison of the Three Parameters of the Numerical Wave Numbers of the GODRP and DRP Schemes

	Parameters		
Schemes	$\overline{\lvert k_r - k\rvert}_{0.4\pi}{}^a$	$\overline{\lvert \theta_r - \theta\rvert}_{0.4\pi}{}^a$	$\overline{\lvert k_i\rvert}_{0.4\pi}{}^a$
GODRP	1.680E-003	0.174	1.414
DRP	1.736E-003	0.225	1.440

$^a\, \overline{|X|}_R = \dfrac{\int_0^R \int_0^\pi |X| r \, d(r)\, d(\theta)}{\int_0^R \int_0^\pi r \, d(r)\, d(\theta)}$.

The physical fluxes are

$$E = [u \;\; p \;\; 0 \;\; u]^t, \quad F = [v \;\; 0 \;\; p \;\; v]^t. \tag{29}$$

The applied boundary conditions are the same as those in the previous simulation using the Cartesian grids.

6.1. Acoustic Wave Propagation

The propagation of a 2-D pressure pulse in the presence of the curvilinear grids is determined. The solution is initialized at $t = 0$ by prescribing a pressure disturbance of the form

$$p = \varepsilon \exp\left[-\ln 2 \cdot \left(\frac{(x - x_0)^2 + (y - y_0)^2}{b^2}\right)\right], \tag{30}$$

where $\varepsilon = 1$, $b = 3$, and $x_0 = y_0 = 0$.

The mesh, shown in Fig. 13A, is generated by Eq. (26) and used for the calculation using the GODRP scheme. For the purpose of comparison, a uniform Cartesian grid is

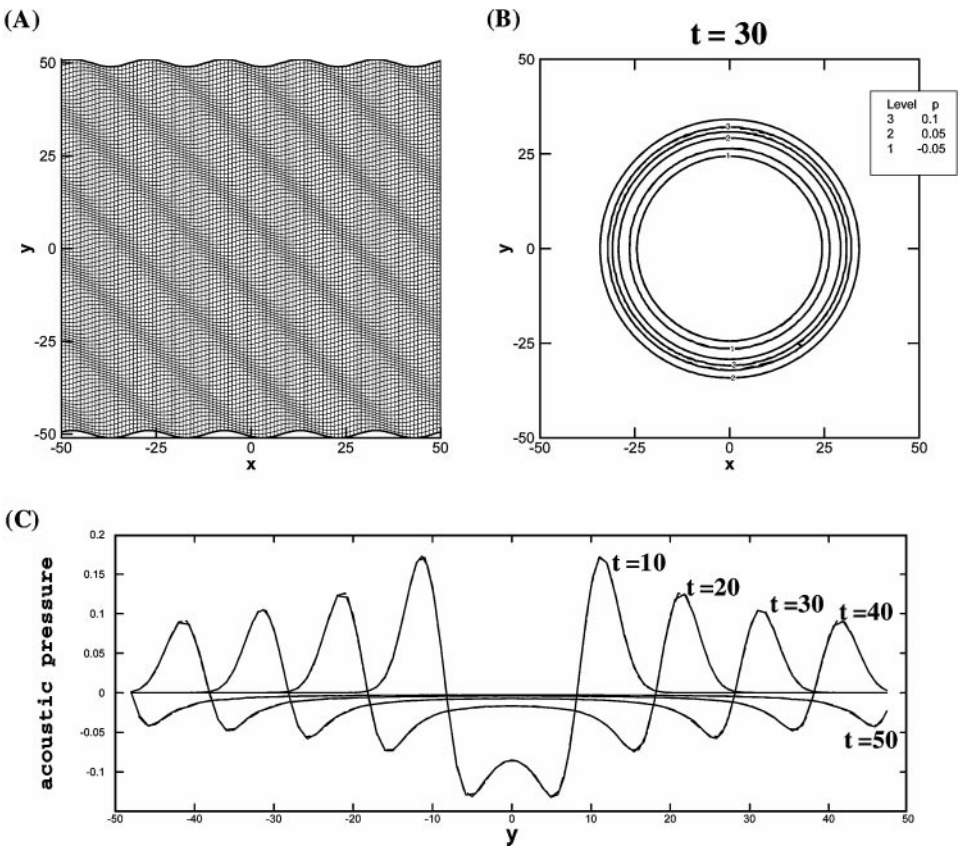

FIG. 13. Comparison of the numerical solutions for the 2-D initial pressure pulse propagation problem. (GODRP scheme, —; DPR scheme, ----). (A) Curvilinear mesh used for the numerical simulation using GODRP schemes. (B) Comparison of pressure contours over the full computational domain at t = 30. (C) Comparison of waveform of acoustic pressure at y-axis at certain time instants.

also considered for the calculation using the DRP scheme. The propagation of the pressure disturbance is computed with $\Delta t = 0.1$ until $t = 5$. By this time, the pressure pulse moves into the boundary region. Figures 13B and C show the pressure contours over the full computational domain and the waveform of the acoustic pressure along the y-axis at some instants, respectively. The figure shows that the solutions of the GODRP scheme show good agreement with those of the DRP scheme on the uniform grids.

6.2. Scattering of Acoustic Pulses from a Cylinder

In order to validate the present approach for curvilinear geometries, we select as a test case the benchmark problem denoted as Category I, problem 2 in the 2nd CAA Workshop [16]. The boundary conditions and the scattering of a prescribed initial pressure pulse off of a circular cylinder at several instants in time for the GODRP scheme are described in Fig. 14. The initial pulse is generated by Eq. (30) with $\varepsilon = 1$, $b = 0.2$, $x_0 = 4$, and $y_0 = 0$. Since the configuration is symmetric, only the upper half of the domain is considered, and symmetry boundary conditions are invoked along $\theta = 0^\circ, 180^\circ$. The dimension of the grid used is 181×201. The values of grid parameters $\Delta r_{max}/D$, $\Delta\theta_{min}$, and $\Delta\theta_{max}$ are 0.056, 0.079 and 0.165, respectively. All cases are advanced in time with a nondimensional Δt of 0.001. At $t = 60$ and $t = 80$, it can be found that there are three wave fronts. The one that is farthest from the cylinder is the wave front created by the initial condition. The next front is a wave reflected off the right surface of the cylinder directly facing the initial pulse. The wave front nearest the cylinder was made when two parts of the initial wave front, separated by the cylinder, collided and merged to the left of the surface of the cylinder.

The histories of pressure at selected points are presented in Fig. 15. The points denoted 'A,' 'B,' and 'C' are located at $(r/D = 5, \theta = 90^\circ)$, $(r/D = 5, \theta = 135^\circ)$, and $(r/D = 5, \theta = 180^\circ)$, respectively. For the comparison, numerical simulations using the GODRP and the DRP schemes on the same grids are executed. Numerical results using both schemes are observed to be in good agreement with the exact solution. But with more detailed inspection

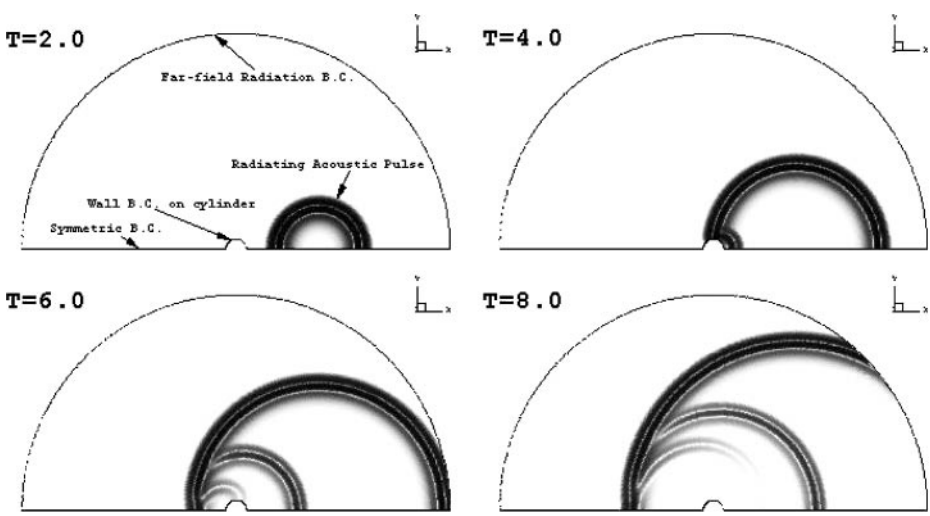

FIG. 14. Boundary conditions applied to the computation and pressure contours at various instants for an acoustic pulse scattered by a circular cylinder.

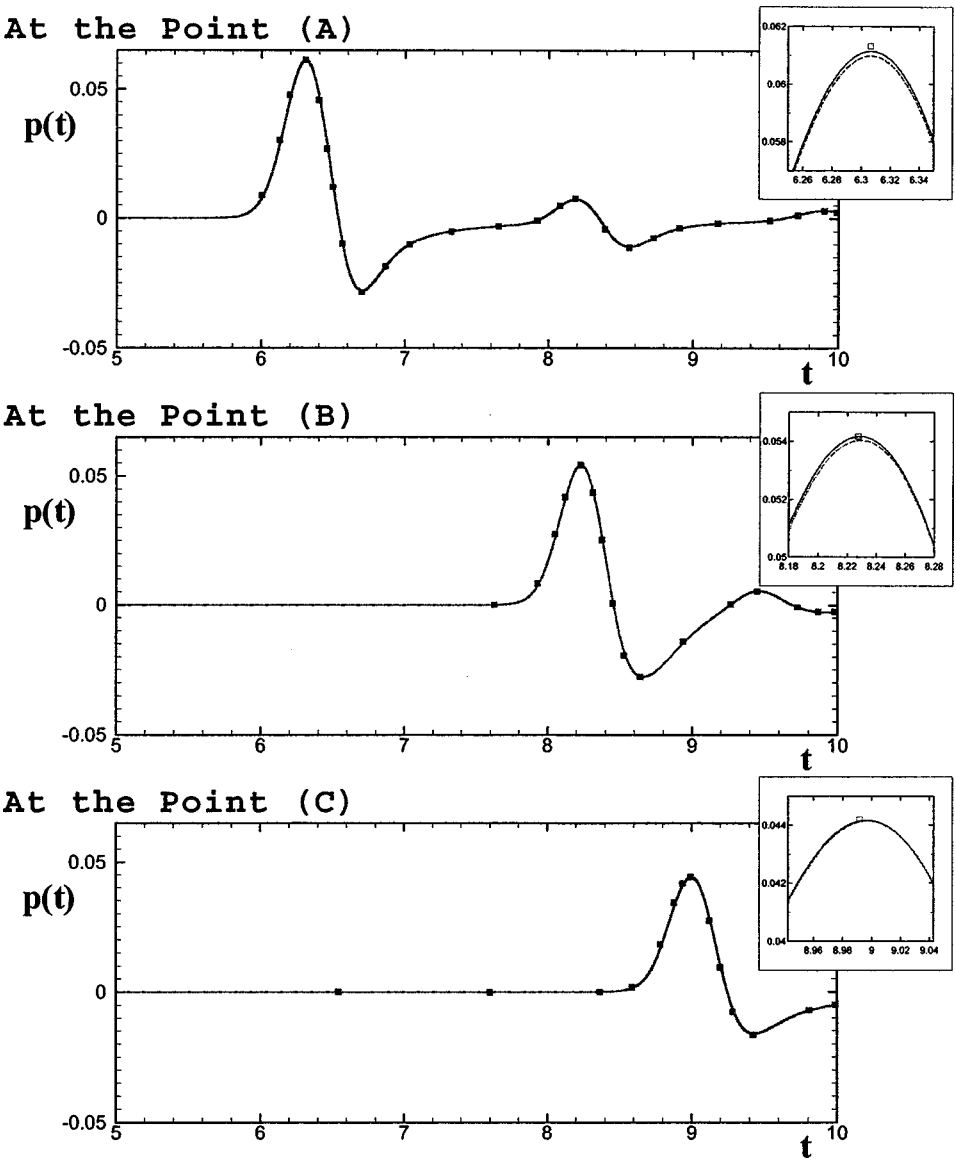

FIG. 15. Time history of pressure fluctuation at selected points. (exact, □; GODRP, —; DRP, · · · · ·).

of the zoomed plots shown in the right portions of Fig. 15, it is found that the results of the GODRP scheme are more accurate than those of the DRP scheme.

7. CONCLUDING REMARKS

Algorithms of grid optimization used to create finite difference equations with the same dispersion relations as the original partial differential equations on general geometries (nonuniform Cartesian and curvilinear meshes) are developed and analyzed. The central idea behind these algorithms is that the optimization processes are carried out not on the computational domain but on the physical domain. Because of the differing properties of Cartesian and curvilinear grids, different optimization algorithms are presented for each

grid type. The effectiveness and accuracy of these schemes are demonstrated in a variety of benchmark problems.

The use of nonuniform Cartesian grids can reduce the number of grid points needed for obtaining accurate numerical solutions. GODRP schemes on nonuniform Cartesian grids can be easily applied in conjunction with multigrid methods. However, centered schemes are favored for their nondissipative property, which is desirable for linear wave propagation. It is thus a recommended strategy to use the GODRP/DRP combined numerical scheme, i.e., to use the DRP scheme on the uniform grid region and the GODRP scheme on the nonuniform area. GODRP schemes of curvilinear grids permit an assessment of the accuracy of the finite difference method for curvilinear meshes from the wave number point of view. Through the grid-optimization process, high-order finite difference equations can be solved with curvilinear grids with a guarantee of local and thus resultant global dispersion-relation-preserving properties.

APPENDIX: ALGORITHM FOR THE DETERMINATION OF THE GODRP STENCIL ON THE CURVILINEAR MESH

By inserting Eq. (23) into Eq. (25), the following integrated error E is obtained:

$$
\begin{aligned}
E = \int_0^R \int_0^\pi \Bigg[& \Bigg(\sum_{j=-n}^{n} a_{\xi,j} (y_\eta)_{l+j,m} \sin(\alpha \Delta x_{l+j,m} \overline{\Delta x} + \beta \Delta y_{l+j,m} \overline{\Delta y}) \cdot \overline{\Delta x} \cdot J \\
& - \sum_{j=-n}^{n} a_{\eta,j} (y_\xi)_{l,m+j} \sin(\alpha \Delta x_{l,m+j} \overline{\Delta x} + \beta \Delta y_{l,m+j} \overline{\Delta y}) \cdot \overline{\Delta x} \cdot J - \alpha \overline{\Delta x} \Bigg)^2 \\
& + \Bigg(- \sum_{j=-n}^{n} a_{\xi,j} (x_\eta)_{l+j,m} \sin(\alpha \Delta x_{l+j,m} \overline{\Delta x} + \beta \Delta y_{l+j,m} \overline{\Delta y}) \cdot \overline{\Delta y} \cdot J \\
& + \sum_{j=-n}^{n} a_{\eta,j} (x_\xi)_{l,m+j} \sin(\alpha \Delta x_{l,m+j} \overline{\Delta x} + \beta \Delta y_{l,m+j} \overline{\Delta y}) \cdot \overline{\Delta y} \cdot J - \beta \overline{\Delta y} \Bigg)^2 \Bigg] \\
& \cdot r \, d(\theta) \, d(r) + \lambda \int_0^R \int_0^\pi \Bigg[- \sum_{j=-n}^{n} a_{\xi,j} (y_\eta)_{l+j,m} \cos(\alpha \Delta x_{l+j,m} \overline{\Delta x} + \beta \Delta y_{l+j,m} \overline{\Delta y}) \\
& \cdot \overline{\Delta x} \cdot J + \sum_{j=-n}^{n} a_{\eta,j} (y_\xi)_{l,m+j} \cos(\alpha \Delta x_{l,m+j} \overline{\Delta x} + \beta \Delta y_{l,m+j} \overline{\Delta y}) \cdot \overline{\Delta x} \cdot J \\
& + \sum_{j=-n}^{n} a_{\xi,j} (x_\eta)_{l+j,m} \cos(\alpha \Delta x_{l+j,m} \overline{\Delta x} + \beta \Delta y_{l+j,m} \overline{\Delta y}) \cdot \overline{\Delta y} \cdot J \\
& - \sum_{j=-n}^{n} a_{\eta,j} (x_\xi)_{l,m+j} \cos(\alpha \Delta x_{l,m+j} \overline{\Delta x} + \beta \Delta y_{l,m+j} \overline{\Delta y}) \cdot \overline{\Delta y} \cdot J \\
& + A \cdot \exp(-\ln 2 \cdot (r - \pi)^2 / \sigma^2) \Bigg]^2 \cdot r \, d(\theta) \, d(r)
\end{aligned}
\tag{A1}
$$

To determine the coefficients of a $2n + 1$-point stencil GODRP spatial discretization in each

direction ξ and η, the Taylor expansions in the computational domain can be utilized to obtain several constraint equations. If two coefficients in each direction are left behind for the optimization, the following $2n-1$ equations are available for each direction:

$$\begin{bmatrix} 1 & 1 & 1 & 1 & 1 & 1 & 1 \\ \Delta_{n-2} & \Delta_{n-3} & \cdots & 0 & \Delta_{-1} & \cdots & \Delta_{-n} \\ \Delta_{n-2}^2 & \Delta_{n-3}^2 & \cdots & 0 & \Delta_{-1}^2 & \cdots & \Delta_{-n}^2 \\ \vdots & \vdots & \vdots & \vdots & \vdots & \vdots & \vdots \\ \Delta_{n-2}^{2n-2} & \Delta_{n-3}^{2n-2} & \cdots & 0 & \Delta_{-1}^{2n-2} & \cdots & \Delta_{-n}^{2n-2} \end{bmatrix} \begin{bmatrix} a_{n-2} \\ a_{n-3} \\ \vdots \\ a_0 \\ a_1 \\ \vdots \\ a_{-n} \end{bmatrix}$$

$$= \begin{bmatrix} -1 \\ -\Delta_n \\ -\Delta_n^2 \\ \vdots \\ -\Delta_n^{2n-2} \end{bmatrix} a_n + \begin{bmatrix} -1 \\ -\Delta_{n-1} \\ -\Delta_{n-1}^2 \\ \vdots \\ -\Delta_{n-1}^{2n-2} \end{bmatrix} a_{n-1} + \begin{bmatrix} 0 \\ 1 \\ 0 \\ \vdots \\ 0 \end{bmatrix}. \tag{A2}$$

Here, Δ_i^k means $sign(i) \cdot (i \times \Delta\xi)^k$ in the ξ-direction and $sign(i) \cdot (i \times \Delta\eta)^k$ in the η-direction. The values of $\Delta\xi$ and $\Delta\eta$ are unity in the computational domain. The above equation can be recast into the following matrix form:

$$\boldsymbol{\Delta X} \cdot \boldsymbol{A} = \boldsymbol{C}_n a_n + \boldsymbol{C}_{n-1} a_{n-1} + \boldsymbol{C}_0. \tag{A3}$$

By multiplying the inverse matrix of $\boldsymbol{\Delta X}$ by both the left- and right-hand sides of the equation, the following equation is obtained:

$$\boldsymbol{A} = \boldsymbol{\Delta X}^{-1} \boldsymbol{C}_n a_n + \boldsymbol{\Delta X}^{-1} \boldsymbol{C}_{n-1} a_{n-1} + \boldsymbol{\Delta X}^{-1} \boldsymbol{C}_0. \tag{A4}$$

The above equation can be rewritten into the following tensor form:

$$a_j = \Delta C_{n,j} a_n + \Delta C_{n-1,j} a_{n-1} + \Delta C_{0,j}. \tag{A5}$$

Here, $a_j = (\boldsymbol{A})_j$, $\Delta C_{n,j} = (\boldsymbol{\Delta X}^{-1} \boldsymbol{C}_n)_j$, $\Delta C_{n-1,j} = (\boldsymbol{\Delta X}^{-1} \boldsymbol{C}_{n-1})_j$, $\Delta C_{0,j} = (\boldsymbol{\Delta X}^{-1} \boldsymbol{C}_0)_j$, in which $(\boldsymbol{M})_j$ represents the *j-th* row element of the matrix $\boldsymbol{M}$. Equation (A5) can be used for both the ξ- and η-directions. By inserting Eq. (A5) into Eq. (A1) and minimizing Eq. (A1), four linear algebraic equations, $\frac{\partial E}{\partial a_{\xi,n}} = 0$, $\frac{\partial E}{\partial a_{\xi,n-1}} = 0$, $\frac{\partial E}{\partial a_{\eta,n}} = 0$, and $\frac{\partial E}{\partial a_{\eta,n-1}}$, are obtained. If a 7-point GODRP stencil is used, the final linear algebraic equations can be expressed as the following matrix form:

$$\boldsymbol{E}_a \cdot \begin{bmatrix} a_{\xi,3} \\ a_{\xi,2} \\ a_{\eta,3} \\ a_{\eta,2} \end{bmatrix} = \boldsymbol{R}. \tag{A6}$$

Here, the elements of the matrixes of $\boldsymbol{E}_a$ and $\boldsymbol{R}$ are defined as

$$(\boldsymbol{E}_a)_{11} = \int_0^R \int_0^\pi [C_3 Y_\eta S \cdot C_3 Y_\eta S + C_3 X_\eta S \cdot C_3 X_\eta S + \lambda (C_3 Y_\eta C + C_3 X_\eta C) \times (C_3 Y_\eta C + C_3 X_\eta C)] \cdot r\, d(r)\, d(\theta)$$

$$(\boldsymbol{E}_a)_{12} = \int_0^R \int_0^\pi [C_2 Y_\eta S \cdot C_3 Y_\eta S + C_2 X_\eta S \cdot C_3 X_\eta S + \lambda (C_2 Y_\eta C + C_2 X_\eta C) \times (C_3 Y_\eta C + C_3 X_\eta C)] \cdot r\, d(r)\, d(\theta)$$

$$(\boldsymbol{E}_a)_{13} = \int_0^R \int_0^\pi [C_3 Y_\xi S \cdot C_3 Y_\eta S + C_3 X_\xi S \cdot C_3 X_\eta S + \lambda (C_3 Y_\xi C + C_3 X_\xi C) \times (C_3 Y_\eta C + C_3 X_\eta C)] \cdot r\, d(r)\, d(\theta)$$

$$(\boldsymbol{E}_a)_{14} = \int_0^R \int_0^\pi [C_2 Y_\xi S \cdot C_3 Y_\eta S + C_2 X_\xi S \cdot C_3 X_\eta S + \lambda (C_2 Y_\xi C + C_2 X_\xi C) \times (C_3 Y_\eta C + C_3 X_\eta C)] \cdot r\, d(r)\, d(\theta)$$

$$(\boldsymbol{E}_a)_{21} = \int_0^R \int_0^\pi [C_3 Y_\eta S \cdot C_2 Y_\eta S + C_3 X_\eta S \cdot C_2 X_\eta S + \lambda (C_3 Y_\eta C + C_3 X_\eta C) \times (C_2 Y_\eta C + C_2 X_\eta C)] \cdot r\, d(r)\, d(\theta)$$

$$(\boldsymbol{E}_a)_{22} = \int_0^R \int_0^\pi [C_2 Y_\eta S \cdot C_2 Y_\eta S + C_2 X_\eta S \cdot C_2 X_\eta S + \lambda (C_2 Y_\eta C + C_2 X_\eta C) \times (C_2 Y_\eta C + C_2 X_\eta C)] \cdot r\, d(r)\, d(\theta)$$

$$(\boldsymbol{E}_a)_{23} = \int_0^R \int_0^\pi [C_3 Y_\xi S \cdot C_2 Y_\eta S + C_3 X_\xi S \cdot C_2 X_\eta S + \lambda (C_3 Y_\xi C + C_3 X_\xi C) \times (C_2 Y_\eta C + C_2 X_\eta C)] \cdot r\, d(r)\, d(\theta)$$

$$(\boldsymbol{E}_a)_{24} = \int_0^R \int_0^\pi [C_2 Y_\xi S \cdot C_2 Y_\eta S + C_2 X_\xi S \cdot C_2 X_\eta S + \lambda (C_2 Y_\xi C + C_2 X_\xi C) \times (C_2 Y_\eta C + C_2 X_\eta C)] \cdot r\, d(r)\, d(\theta)$$

$$(\boldsymbol{E}_a)_{31} = \int_0^R \int_0^\pi [C_3 Y_\eta S \cdot C_3 Y_\xi S + C_3 X_\eta S \cdot C_3 X_\xi S + \lambda (C_3 Y_\eta C + C_3 X_\eta C) \times (C_3 Y_\xi C + C_3 X_\xi C)] \cdot r\, d(r)\, d(\theta)$$

$$(\boldsymbol{E}_a)_{32} = \int_0^R \int_0^\pi [C_2 Y_\eta S \cdot C_3 Y_\xi S + C_2 X_\eta S \cdot C_3 X_\xi S + \lambda (C_2 Y_\eta C + C_2 X_\eta C) \times (C_3 Y_\xi C + C_3 X_\xi C)] \cdot r\, d(r)\, d(\theta)$$

$$(\boldsymbol{E}_a)_{33} = \int_0^R \int_0^\pi [C_3 Y_\xi S \cdot C_3 Y_\xi S + C_3 X_\xi S \cdot C_3 X_\xi S + \lambda (C_3 Y_\xi C + C_3 X_\xi C) \times (C_3 Y_\xi C + C_3 X_\xi C)] \cdot r\, d(r)\, d(\theta)$$

$$(\boldsymbol{E}_a)_{34} = \int_0^R \int_0^\pi [C_2 Y_\xi S \cdot C_3 Y_\xi S + C_2 X_\xi S \cdot C_3 X_\xi S + \lambda (C_2 Y_\xi C + C_2 X_\xi C) \times (C_3 Y_\xi C + C_3 X_\xi C)] \cdot r\, d(r)\, d(\theta)$$

$$(\boldsymbol{E}_a)_{41} = \int_0^R \int_0^\pi [C_3 Y_\eta S \cdot C_2 Y_\xi S + C_3 X_\eta S \cdot C_2 X_\xi S + \lambda (C_3 Y_\eta C + C_3 X_\eta C) \times (C_2 Y_\xi C + C_2 X_\xi C)] \cdot r\, d(r)\, d(\theta)$$

$$(\boldsymbol{E}_a)_{42} = \int_0^R \int_0^\pi [C_2 Y_\eta S \cdot C_2 Y_\xi S + C_2 X_\eta S \cdot C_2 X_\xi S + \lambda (C_2 Y_\eta C + C_2 X_\eta C) \times (C_2 Y_\xi C + C_2 X_\xi C)] \cdot r\, d(r)\, d(\theta)$$

$$
\begin{aligned}
(\boldsymbol{E}_a)_{43} &= \int_0^R \int_0^\pi [C_3Y_\xi S \cdot C_2Y_\xi S + C_3X_\xi S \cdot C_2X_\xi S + \lambda(C_3Y_\xi C + C_3X_\xi C) \\
&\quad \times (C_2Y_\xi C + C_2X_\xi C)] \cdot r\,d(r)\,d(\theta) \\
(\boldsymbol{E}_a)_{44} &= \int_0^R \int_0^\pi [C_2Y_\xi S \cdot C_2Y_\xi S + C_2X_\xi S \cdot C_2X_\xi S + \lambda(C_2Y_\xi C + C_2X_\xi C) \\
&\quad \times (C_2Y_\xi C + C_2X_\xi C)] \cdot r\,d(r)\,d(\theta) \\
(\boldsymbol{R})_1 &= -\int_0^R \int_0^\pi [(C_0Y_\eta S + C_0Y_\xi S - \alpha\overline{\Delta x}) \cdot C_3Y_\eta S + (C_0X_\eta S + C_0X_\xi S - \beta\overline{\Delta y}) \\
&\quad \cdot C_3X_\eta S + \lambda(C_0Y_\eta C + C_0Y_\xi C + C_0X_\eta C + C_0X_\xi C \\
&\quad - A \cdot \mathrm{EXP}(-\ln 2 \cdot (r-\pi)^2/\sigma^2)) \cdot (C_3Y_\eta C + C_3X_\eta C)] \cdot r\,d(r)\,d(\theta) \\
(\boldsymbol{R})_2 &= -\int_0^R \int_0^\pi [(C_0Y_\eta S + C_0Y_\xi S - \alpha\overline{\Delta x}) \cdot C_2Y_\eta S + (C_0X_\eta S + C_0X_\xi S - \beta\overline{\Delta y}) \\
&\quad \cdot C_2X_\eta S + \lambda(C_0Y_\eta C + C_0Y_\xi C + C_0X_\eta C + C_0X_\xi C \\
&\quad - A \cdot \mathrm{EXP}(-\ln 2 \cdot (r-\pi)^2/\sigma^2)) \cdot (C_2Y_\eta C + C_2X_\eta C)] \cdot r\,d(r)\,d(\theta) \\
(\boldsymbol{R})_3 &= -\int_0^R \int_0^\pi [(C_0Y_\eta S + C_0Y_\xi S - \alpha\overline{\Delta x}) \cdot C_3Y_\xi S + (C_0X_\eta S + C_0X_\xi S - \beta\overline{\Delta y}) \\
&\quad \cdot C_3X_\xi S + \lambda(C_0Y_\eta C + C_0Y_\xi C + C_0X_\eta C + C_0X_\xi C \\
&\quad - A \cdot \mathrm{EXP}(-\ln 2 \cdot (r-\pi)^2/\sigma^2)) \cdot (C_3Y_\xi C + C_3X_\xi C)] \cdot r\,d(r)\,d(\theta) \\
(\boldsymbol{R})_4 &= -\int_0^R \int_0^\pi [(C_0Y_\eta S + C_0Y_\xi S - \alpha\overline{\Delta x}) \cdot C_2Y_\xi S + (C_0X_\eta S + C_0X_\xi S - \beta\overline{\Delta y}) \\
&\quad \cdot C_2X_\xi S + \lambda(C_0Y_\eta C + C_0Y_\xi C + C_0X_\eta C + C_0X_\xi C \\
&\quad - A \cdot \mathrm{EXP}(-\ln 2 \cdot (r-\pi)^2/\sigma^2)) \cdot (C_2Y_\xi C + C_2X_\xi C)] \cdot r\,d(r)\,d(\theta),
\end{aligned}
$$

where

$$
\begin{aligned}
C_fY_\eta S &= \sum_{j=-3}^{3} \Delta C_{f,j}(y_\eta)_{n+j,m} \sin(\alpha\Delta x_{n+j,m}\overline{\Delta x} + \beta\Delta y_{n+j,m}\overline{\Delta y}) \cdot \overline{\Delta x} \cdot J, \\
C_fX_\eta S &= -\sum_{j=-3}^{3} \Delta C_{f,j}(x_\eta)_{n+j,m} \sin(\alpha\Delta x_{n+j,m}\overline{\Delta x} + \beta\Delta y_{n+j,m}\overline{\Delta y}) \cdot \overline{\Delta y} \cdot J, \\
C_fY_\eta C &= -\sum_{j=-3}^{3} \Delta C_{f,j}(y_\eta)_{n+j,m} \cos(\alpha\Delta x_{n+j,m}\overline{\Delta x} + \beta\Delta y_{n+j,m}\overline{\Delta y}) \cdot \overline{\Delta x} \cdot J, \\
C_fX_\eta C &= \sum_{j=-3}^{3} \Delta C_{f,j}(x_\eta)_{n+j,m} \cos(\alpha\Delta x_{n+j,m}\overline{\Delta x} + \beta\Delta y_{n+j,m}\overline{\Delta y}) \cdot \overline{\Delta y} \cdot J, \\
C_fY_\xi S &= -\sum_{j=-3}^{3} \Delta C_{f,j}(y_\xi)_{n,m+j} \sin(\alpha\Delta x_{n+j,m}\overline{\Delta x} + \beta\Delta y_{n+j,m}\overline{\Delta y}) \cdot \overline{\Delta x} \cdot J, \\
C_fX_\xi S &= \sum_{j=-3}^{3} \Delta C_{f,j}(x_\xi)_{n,m+j} \sin(\alpha\Delta x_{n+j,m}\overline{\Delta x} + \beta\Delta y_{n+j,m}\overline{\Delta y}) \cdot \overline{\Delta y} \cdot J,
\end{aligned}
$$

$$C_f Y_\xi C = \sum_{j=-3}^{3} \Delta C_{f,j}(y_\xi)_{n,m+j} \cos(\alpha \Delta x_{n+j,m} \overline{\Delta x} + \beta \Delta y_{n+j,m} \overline{\Delta y}) \cdot \overline{\Delta x} \cdot J,$$

$$C_f X_\xi C = -\sum_{j=-3}^{3} \Delta C_{f,j}(x_\xi)_{n,m+j} \cos(\alpha \Delta x_{n+j,m} \overline{\Delta x} + \beta \Delta y_{n+j,m} \overline{\Delta y}) \cdot \overline{\Delta y} \cdot J.$$

The values of the coefficients of $a_{\xi,3}$, $a_{\xi,2}$, $a_{\eta,3}$, and $a_{\eta,2}$ can be determined by solving Eq. (A6) at a given grid point. The values of the other coefficients, $a_{\xi,j}$ ($j = 1, 0, -1, -2, -3$) and $a_{\eta,j}$ ($j = 1, 0, -1, -2, -3$) can then be set using Eq. (A2).

The data of grid spacing and the optimized coefficients, which are used for the calculations shown in Fig. 11, Fig. 12, and Table II, are as follows:

$$\overline{\Delta x} = 1.0, \quad \overline{\Delta y} = 0.781830500937500$$
$$\Delta x_{n+3,m} = 3.0, \quad \Delta x_{n,m+3} = 0.0,$$
$$\Delta y_{n+3,m} = -1.14705456693252, \quad \Delta y_{n,m+3} = 2.69009427338859$$
$$\Delta x_{n+2,m} = 2.0, \quad \Delta x_{n,m+2} = 0.0,$$
$$\Delta y_{n+2,m} = -0.751806499730670, \quad \Delta y_{n,m+2} = 1.80629272715007$$
$$\Delta x_{n+1,m} = 1.0, \quad \Delta x_{n,m+1} = 0.0,$$
$$\Delta y_{n+1,m} = -0.356558432528822, \quad \Delta y_{n,m+1} = 0.922491180911548$$
$$\Delta x_{n,m} = 0.0, \quad \Delta x_{n,m} = 0.0, \quad \Delta y_{n,m} = 0.0, \quad \Delta y_{n,m} = 0.0$$
$$\Delta x_{n-1,m} = -1.0, \quad \Delta x_{n,m-1} = 0.0,$$
$$\Delta y_{n-1,m} = 0.282966374191363, \quad \Delta y_{n,m-1} = -0.996083239249006$$
$$\Delta x_{n-2,m} = -2.0, \quad \Delta x_{n,m-2} = 0.0,$$
$$\Delta y_{n-2,m} = 0.464641969796655, \quad \Delta y_{n,m-2} = -2.09345725708408$$
$$\Delta x_{n-3,m} = -3.0, \quad \Delta x_{n,m-3} = 0.0,$$
$$\Delta y_{n-3,m} = 0.527243113709700, \quad \Delta y_{n,m-3} = -3.30990572661141$$
$$a_{\xi,3} = 2.155844360735511\text{E-}002, \quad a_{\eta,3} = 3.912413002055540\text{E-}002$$
$$a_{\xi,2} = -0.170871362842768, \quad a_{\eta,2} = -0.262703436013810$$
$$a_{\xi,1} = 0.780980160103516, \quad a_{\eta,1} = -0.228735825982549$$
$$a_{\xi,0} = -1.304255080014649\text{E-}002, \quad a_{\eta,0} = -0.633551490786896$$
$$a_{\xi,-1} = -0.761416333903296, \quad a_{\eta,-1} = 0.976655229760718$$
$$a_{\xi,-2} = 0.163045832362681, \quad a_{\eta,-2} = 0.125461940424281$$
$$a_{\xi,-3} = -2.025418852734050\text{E-}002, \quad a_{\eta,-3} = -1.625054742230063\text{E-}002.$$

Backward and forward finite difference schemes are used near the boundaries where all the points are not available for central differencing. The above optimization process can be applied to the boundary stencil, except that different formulas are needed instead of Eq. (A2). The formal order of accuracy of the boundary stencil is the same as that of the central difference. The stability is also retained through the optimization process of the imaginary part of the numerical wave number.

ACKNOWLEDGMENT

This work was sponsored by the Research Institute of Engineering Science and the Brain Korea 21 Project.

REFERENCES

1. J. C. Hardin, J. R. Ristorcelli, and C. K. W. Tam, ICASE/LaRC workshop on benchmark problems in computational aeroacoustics, *NASA CP 3300* (1995).
2. R. Hixon, Evaluation of a high-accuracy MacCormack-type scheme using benchmark problems, *J. Comput. Acoust.* **6**, 291 (1998).
3. R. Hixon and E. Turkel, Compact implicit MacCormack-type schemes with high accuracy, *J. Comput. Phys.* **158**, 51 (2000).
4. S. Y. Lin and Y. S. Chen, Comparison of higher resolution Euler schemes for aeroacoustic computations, *AIAA J.* **33**, 237 (1995).
5. S. Y. Lin and Y. S. Chen, Numerical study of MUSCL schemes for computational aeroacoustics, *AIAA paper* 97-0023 (1987).
6. L. N. Sankar, N. N. Reddy, and N. Hariharan, A third order upwind scheme for aeroacoustic application, *AIAA paper* 93-0149 (1993).
7. X. Deng and H. Zhang, Developing high-order weighted compact nonlinear schemes, *J. Comput. Phys.* **165**, 1 (2000).
8. C. K. W. Tam, Computational aeroacoustics: Issues and methods, *AIAA J.* **33**, 1788 (1995).
9. V. L. Wells and R. A. Renaut, Computing aerodynamically generated noise, *Annu. Rev. Fluid Mech.* **29**, 161 (1997).
10. S. K. Lele, Compact finite difference schemes with spectral-like resolution, *J. Comput. Phys.* **103**, 16 (1992).
11. C. K. W. Tam and J. C. Webb, Dispersion-relation-preserving schemes for computational acoustics, *J. Comput. Phys.* **107**, 262 (1993).
12. D. V. Nance, K. Viswanathan, and L. N. Sankar, Low-dispersion finite volume scheme for aeroacoustic applications, *AIAA J.* **35**, 255 (1997).
13. M. Zhuang and R. F. Chen, Optimized upwind dispersion-relation-preserving finite difference scheme for computational aeroacoustics, *AIAA J.* **36**, 2146 (1998).
14. J. Casper, C.-W. Shu, and H. Atkins, Comparison of two formulations for high-order accurate essentially nonoscillatory schemes, *AIAA J.* **32**, 1970 (1994).
15. R. Vichnevetsky and J. B. Bowles, *Fourier Analysis of Numerical Approximations of Hyperbolic Equations* (Soc. For Indus. & Appl. Math., Philadelphia, 1982).
16. C. K. W. Tam and J. C. Hardin, Second computational aeroacoustics workshop on benchmark problems, *NASA CP 3352* (1997).
17. P. J. Morris, L. N. Long, A. Bangalore, and Q. Wang, A parallel three-dimensional computational aeroacoustics method using nonlinear disturbance equations, *J. Comput. Phys.* **133**, 56 (1997).
18. T. Z. Dong, S. H. Shih, R. R. Mankbadi, and L. A. Povinelli, A numerical study of duct geometry effect on radiation of engine internal noise, 3rd AIAA/CEAS A. C., AIAA-97-1604 (1997).
19. C. K. W. Tam and Z. Dong, Radiation and outflow boundary conditions for direct computation of acoustic and flow disturbances in a nonuniform mean flow, *J. Comput. Acoust.* **4**, 175 (1996).
20. C. K. W. Tam and Z. Dong, Wall boundary condition for high-order finite difference schemes in computational aeroacoustics, *Theor. Comput. Fluid Dyn.* **8**, 303 (1994).
21. R. Vichnevetsky, Propagation through numerical mesh refinement for hyperbolic equations, *Math. Comp. Simul.* **23**, 344 (1981).
22. C. Cheong and S. Lee, The effects of discontinuous boundary conditions on the directivity of sound from a piston, *J. Sound Vib.* **239**, 423 (2001).